Origin and evolution of gold-bearing fluids in a carbon-rich sedimentary basin: A case study of the Algamarca epithermal gold-silver-copper deposit, northern Peru

Renzo Galdos [a,b], Jean Vallance [a], Patrice Baby [b,c], Stefano Salvi [b], Michael Schirra [d], German Velasquez [e], Willem Viveen [c], Rodrigo Soto [a], Gleb S. Pokrovski [b,*]

[a] *Grupo de investigación en Geología de Yacimientos, Especialidad de Ingeniería Geológica, Departamento de Ingeniería, Pontificia Universidad Católica del Perú, avenida Universitaria 1801, San Miguel, Lima 15088, Peru*
[b] *Géosciences Environnement Toulouse, Université Toulouse III – Paul Sabatier, CNRS, IRD, CNES, OMP, 14 avenue Edouard Belin, F-31400 Toulouse, France*
[c] *Grupo de investigación en Geología Sedimentaria, Especialidad de Ingeniería Geológica, Departamento de Ingeniería, Pontificia Universidad Católica del Perú, avenida Universitaria 1801, San Miguel, Lima 15088, Peru*
[d] *Department of Earth Sciences, University of Geneva, 1205 Geneva, Switzerland*
[e] *Instituto de Geología Económica Aplicada, Universidad de Concepción, casilla 160-C, Concepción, Chile*

ARTICLE INFO

ABSTRACT

Sediment-hosted gold deposits account for the major part of economic gold in the Earth's crust. However, the origin of the gold-bearing fluid and its evolution in sedimentary basins in the presence of organic carbon and its metamorphosed products such as graphite are poorly known. In an attempt to clarify these issues, we performed an integrated mineralogical, geochemical, and fluid-inclusion study of the Algamarca epithermal Au-Ag-Cu deposit, hosted by Mesozoic sediments corresponding to an over-mature petroleum system within the Marañón fold and thrust belt (northern Peru). Results show that mineralization started with a pre-gold stage characterized by quartz veins containing gold-poor pyrite and chalcopyrite. Most gold was deposited afterwards, during the main gold stage in an "invisible" form within arsenian pyrite, followed by minor visible native gold with sulfosalts and chalcopyrite at a later stage. Fluid inclusions in quartz from the pre-gold and gold stages show features analogous to those observed in porphyry Cu-Au systems such as vapor–liquid immiscibility, enrichment in K, Rb, Cu, As, and Sb, a wide range of salinity (5–35 wt% NaCl eq.), and similar elemental (atomic) ratios (Zn/Pb ~ 4, 0.1 < K/Na < 5, Br/Cl ~ 0.06), all consistent with a fluid of magmatic origin. In addition, the fluid inclusions from the pre-gold stage are highly enriched in CO_2 (~60 mol% in gas phase), CH_4 (~10 mol%) and H_2S (~30 mol%). Such high volatile contents are rather unusual for typical porphyry-epithermal systems and likely reflect reactions between the magmatic fluid and carbon-bearing sediments. This conclusion is independently supported by the temperature values of graphite metamorphic peak determined by Raman spectroscopy, which are similar to those derived by fluid-inclusion microthermometry in quartz veins. Our findings imply that strong interactions of magmatic fluid with carbonaceous matter favored gold transport through the sedimentary basin and its subsequent concentration in arsenian pyrite. Furthermore, our results point to a possible presence of porphyry-style mineralization beneath the sedimentary sequence hosting the epithermal Algamarca deposit, thereby providing new potential for exploration.

1. Introduction

The ubiquitous presence of carbonaceous material, such as graphite, bitumen, pyrobitumen, and hydrocarbons, and their close association with gold-rich arsenian pyrite are two key ingredients shared by many types of sedimentary-hosted gold deposits including Carlin, orogenic, and some epithermal types, not to mention the largest gold anomaly on Earth - Witwatersrand (Arehart, 1996; Cline et al., 2005; Large et al., 2011, 2013; Agangi et al., 2013, 2015; Vaughan et al., 2020; Wu et al., 2020; Fuchs et al., 2021; Gaboury et al., 2021; Ge et al., 2022; Ding

et al., 2023; Vallance et al., 2024). These deposits correspond to the major world's known gold endowments; a single deposit or province can contain tens to hundreds million ounces of gold (e.g., Muntean et al., 2011; Frimmel and Nwaila, 2020). Consequently, these deposits have been in the focus of a large volume of scientific literature, leading to their structural, petrological, and mineralogical frameworks being well characterized. In contrast, considerably less effort has been allocated to delving into the genesis of mineralizing fluids and their evolution within sedimentary basins. The major enigmatic issue is the involvement of carbonaceous material and arsenic-rich pyrite in the transportation and concentration of gold, ultimately promoting its deposition. Despite various proposed models aiming to address this issue, the role played by both parameters is still controversial and subject of ongoing debate. Some of these models suggest that metamorphic or basinal fluids may reconcentrate gold from sedimentary or metasedimentary rocks (e.g., Hofstra and Cline, 2000; Large et al., 2011; Large et al., 2013), while others emphasize the importance of an external mineralizing input, such as magmatic fluids (e.g., Sillitoe and Bonham, 1990; Barker et al., 2009; Muntean et al., 2011; Large et al., 2016; Vallance et al., 2024). The consensus regarding the role played by carbonaceous material equally remains elusive. While it is generally assumed that interactions of hydrothermal fluids with organic matter trigger gold precipitation due to reduction (e.g., Radtke and Scheiner, 1970), other studies have demonstrated that such interactions actually enhance gold solubility (Vallance et al., 2024). Likewise, gold transport by organic fluids, such as petroleum, has received limited attention, with only a handful of studies dedicated to this subject demonstrating fairly modest gold solubility compared to that in S-bearing aqueous solution (e.g., Pokrovski et al., 2014; Crede et al., 2019). The resolution of this debate is hindered by several factors. Firstly, the intricate metallogenic evolution observed in the majority of deposits, characterized by the superimposition of various mineralization events, poses difficulties in establishing a clear sequence of ore-forming stages solely through mineralogical observation and geochronological dating (e.g., Groves et al., 2003; Cline et al., 2005; Emsbo et al., 2006; Vikentyev et al., 2019; Seltmann et al., 2020; Vursiy et al., 2020). Secondly, direct evidence from fluid inclusions remains rare for sediment-hosted gold deposits. This scarcity can be attributed to the limited presence of quartz, as well as its fine-grained texture in many sediment-hosted hydrothermal settings that results both in overly small size (e.g., <2–10 μm in Carlin type deposits from Nevada; Hofstra and Cline, 2000; Large et al., 2016; references therein) and limited availability of fluid inclusions (e.g., Cline et al., 2005; Pinet et al., 2023; Vallance et al., 2024). Although quartz is much more abundant in orogenic-type deposits, good preservation state of fluid inclusions is unusual (Zhang and Audétat, 2023), and in many cases fluid inclusions are also very small (typically < 5 μm; e.g., Velásquez et al., 2014). These conditions pose analytical challenges for in-situ LA-ICPMS analyses of fluid inclusions (e.g., Cline et al., 2005; Deditius et al., 2014). This paucity of direct information on the ore-forming fluid in sedimentary basins contrasts with the large amount of fluid-inclusion data available from magmatic-hydrothermal porphyry systems (e.g., Kouzmanov and Pokrovski, 2012; references therein). Alternatively, certain sulfide minerals, such as pyrite, sphalerite, enargite, wolframite and stibnite, which are opaque when observed under transmitted light in the visible spectral region, can be examined using infrared microscopy to identify any fluid inclusions they may contain (e.g., Campbell and Robinson-Cook, 1987; Richards and Kerrich, 1993; Moritz, 2006; Kouzmanov et al., 2002; Ortelli et al., 2018). Such study can be combined with in-situ LA-ICPMS analyses to determine their bulk composition (e.g., Kouzmanov et al., 2010; Rottier et al., 2018). However, analyzing fluid inclusions in opaque As-bearing minerals presents significant challenges, primarily due to the considerable infrared radiation absorption caused by arsenic, a prevalent element commonly found in pyrite associated with these gold deposits.

In light of the above challenges, our study offers a unique opportunity to investigate mineralizing hydrothermal fluids within an organic carbon-rich sedimentary basin, focusing on the Algamarca epithermal deposit. Consisting of Au-Ag-Cu veins of Miocene age, this relatively young deposit offers a simplified sequence of mineralization events, encompassing only three hypogene stages of ore deposition. The veins consist predominantly of quartz, which serves as the primary host for abundant fluid inclusions of suitable size for a range of analyses (microthermometry, Raman spectroscopy and LA-ICPMS). While extensive research has been conducted on other epithermal Au-Ag deposits hosted by Cretaceous sedimentary rocks like Lagunas Norte, Shahuindo and La Arena in the Marañón fold and thrust belt (MFTB) of northern Peru, these studies were primarily focused on geochronological dating, mineralogical and geochemical characterization and stable isotope analyses (e.g., Montgomery, 2012; Cerpa et al., 2013; Santos et al., 2023; Vallance et al., 2024). To the best of our knowledge, no studies have been published specifically targeting the characterization of mineralizing fluids in these deposits.

In this paper, we present a comprehensive analysis of the properties and composition of the mineralizing fluids, textural and compositional characteristics of pyrite and quartz, a detailed paragenetic sequence, as well as a metallogenic model for the Algamarca deposit. Our work is based on meticulous sampling campaigns, systematic mineralogical studies, and rigorous in-situ analyses of minerals and fluid inclusions. The outcomes of our investigation offer novel insights into the origin and evolution of the mineralizing fluids within an organic carbon-rich basin. Additionally, our findings demonstrate the efficiency of detailed in-situ determination of major and trace elements as a viable approach for identifying concealed porphyry-style mineralization beneath the epithermal mineralization.

1.1. Geological setting

1.1.1. Regional geology

The Algamarca Au-Ag-Cu deposit is situated in the Marañón fold and thrust belt, in the Andes of northern Peru. The MFTB hosts a suite of epithermal, porphyry and skarn deposits associated with subduction-related Oligo-Miocene magmatic arc intrusions and belongs to the Miocene metallogenic belt of central and northern Peru (Noble and McKee, 1999; Scherrenberg et al., 2016). Remarkable deposits currently being mined include Yanacocha, Lagunas Norte, and Shahuindo (all epithermal-type), and Antamina (skarn-type), to name a few. The fertility of the belt has been attributed to a change in the subduction geometry (from normal to flat slab) triggered by the subduction of the Nazca ridge and Inca plateau (topographic anomalies) between 15 Ma and 13 Ma (Rosenbaum et al., 2005; Cooke et al., 2005).

The MFTB is an essential structural component of the western Cordillera of the Andes. It corresponds to an east-verging thin-skinned thrust system, which propagated in a fluvio-deltaic and marine sedimentary series, late Jurassic to late Cretaceous in age. The sediments were deposited in a back-arc basin on a basement formed by metamorphic rocks from Precambrian to lower-Ordovician, known as the Marañón complex (Mégard, 1984; Benavides-Cáceres, 1999; Chew et al., 2007; Scherrenberg et al., 2016). The MFTB developed during an early period of the Andean orogeny (traditionally known as the Peruvian and Incaic phases; Noble et al., 1979; Mégard, 1984), between the late Cretaceous and the middle Eocene. The main décollement occurred at the interface between the Mesozoic series and the basement, in the late Jurassic black shales of the Chicama Formation (Mégard, 1984; Jaillard and Jacay, 1989; Eude et al., 2015). The MFTB is truncated by a middle Eocene regional unconformity sealed by volcanic and volcano-clastic sediments of the late Eocene to middle Miocene Calipuy plateau-basin (Cossio and Jaen, 1967; Noble et al.,1990; Prudhomme et al., 2019). The western Cordillera and MFTB have been uplifted at their current altitude (from ~3000 to 4000 m a.s.l.) during the Neogene orogenic period.

1.1.2. Geology of the Algamarca deposit

The Algamarca deposit is hosted by the Algamarca anticline, a well-preserved and prominent structure situated in the northern part of the MFTB (Fig. 1a, b), 22 km west of Cajabamba town and ~1 km northwest of the Shahuindo deposit (Fig. 1a-c), at a current elevation of 3100 m a.s. l. It consists of veins trending perpendicularly or obliquely to the anticline axis. Stratigraphically, the Algamarca anticline is composed by the late Jurassic black shales with intercalations of fine-grained sandstone of the Chicama Formation and the overlying lower Cretaceous fluvio-deltaic and shallow-marine sequences of the Goyllarisquizga Group (Benavides-Cáceres, 1956; Navarro et al., 2010; Defilippi et al., 2016). The Goyllarisquizga Group includes, from bottom to top, quartz-rich massive sandstone with minor intercalations of shale, siltstone and coal bed of the Chimú Formation, black shales with lenticular siltstones, minor mudstones and limestones of the Santa Formation, interbedded siltstone, mudstone, and sandstone of the Carhuaz Formation, and quartz-rich sandstone with minor interbedded siltstone of the Farrat Formation (Fig. 2). Sandstones from the Chimú, Carhuaz, and Farrat formations are the main country rocks for the epithermal mineralization in the district including the Algamarca deposit (Fig. 1a; Gauthier et al., 1999; Defilippi et al., 2016). Oligocene-Miocene andesitic and dacitic intrusive stocks were emplaced at the intersection of NW-SE thrust faults and later NE-SW transverse faults, or along the axis of the Algamarca anticline (Fig. 1b, c; Defilippi et al., 2016; Vallance et al., 2024). They outcrop in the area and were intercepted by underground workings of the Algamarca mine. The Algamarca deposit has been exploited since Spanish colonial times. Later, Minera Algamarca SA operated an underground mine between 1945 and 1989 (Wright et al., 2009; Tietz and Defilippi, 2012). Some veins are currently mined on a small scale by AMASBA artisanal miners' association.

The Algamarca deposit is composed by seven veins labelled as Descubridora, San Blas, Los Alisos, Rosario, Lucy, Concepción, and
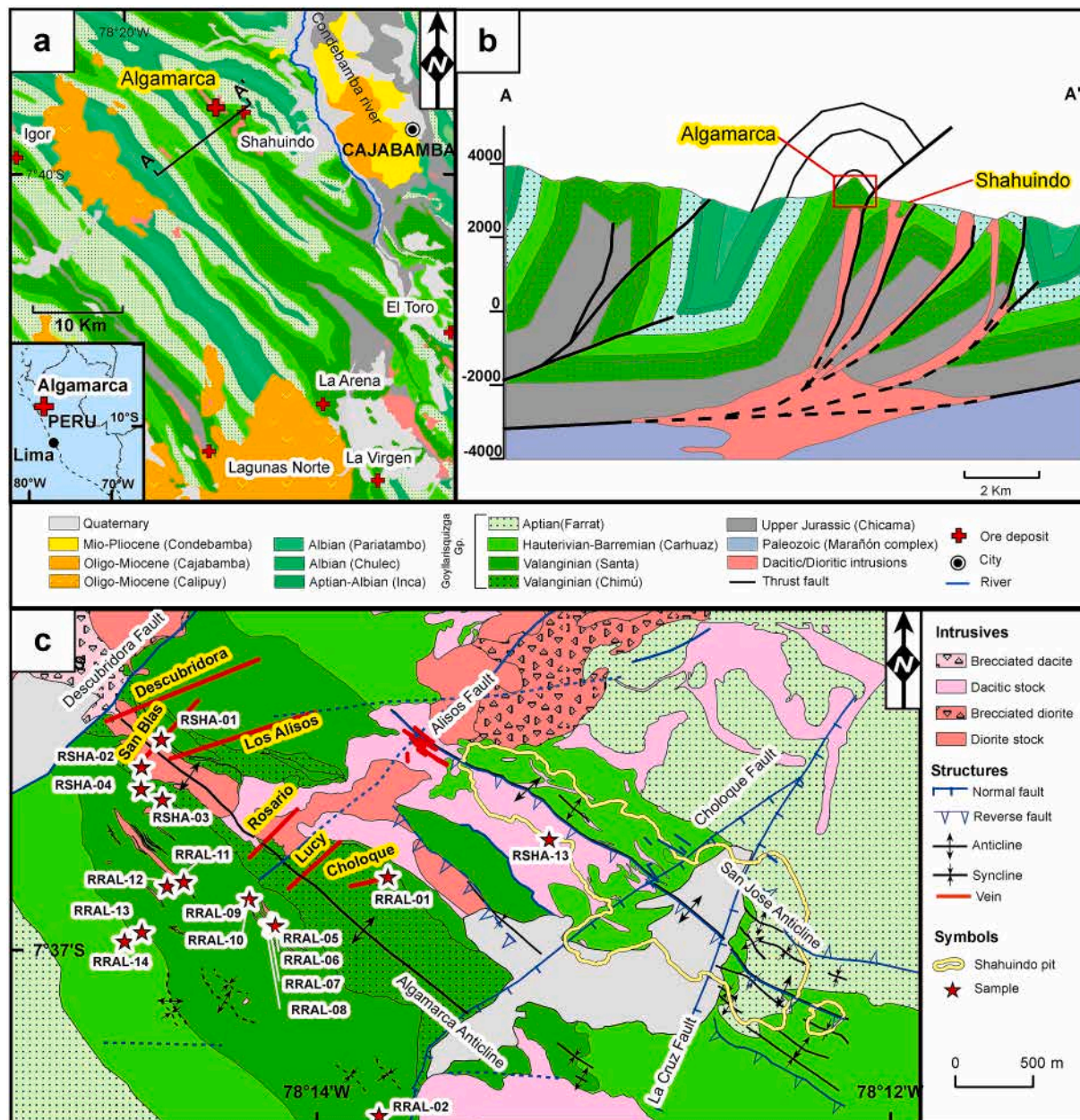

Fig. 1. (a) Regional geological map showing the principal ore deposits in the north of the Marañón fold and thrust belt, and location of the A-Á cross section depicted in 1b (modified after INGEMMET, 2017). (b) Structural SW-NE cross section (modified after Vallance et al., 2024). (c) Local geology of the Algamarca deposit. Note that the Lucy and Concepción veins overlap on the map. The location of the Shahuindo open pit is also shown (modified after Defilippi et al., 2016).
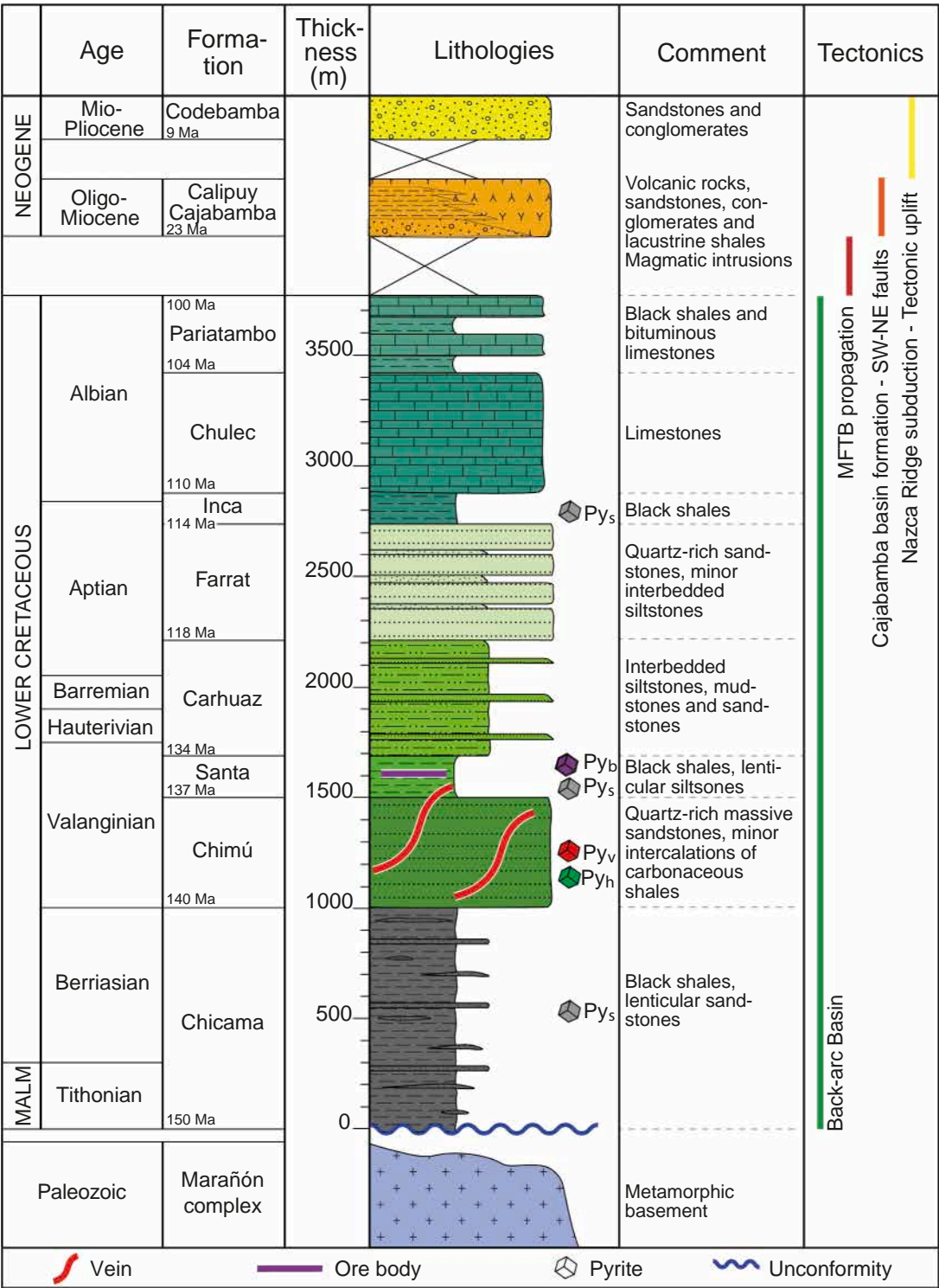
Fig. 2. Stratigraphical column of the Marañón fold and thrust belt in the study area (modified after Vallance et al., 2024), also showing the position of the Algamarca veins, ore bodies and different pyrite types. Abbreviations for pyrites types are as in Table 2.

Choloque, all of them of thicknesses varying from 0.1 to 2 m, up to more than 600 m in length, and extending over about 200 m in the vertical direction. The veins strike northeast and dip 60° to 70° to southeast (Fig. 1c; Defilippi et al., 2016). Maximum vein thicknesses are observed in the more competent lithologies such as quartzite of the Chimú Formation and andesitic intrusive stocks. In contrast, in less competent rocks, like coal beds of the Chimú Formation and shales of the Santa Formation, veins tend to split into fine branches of less than 1 cm thick

(Defilippi et al., 2016). Grades of up to 14 g/t Au, 2700 g/t Ag, and 25 wt % Cu were reported from one-sampling analyses in the Descubridora vein (the most exploited at Algamarca), which is hosted by quartz-rich sandstones of the Chimú Formation (Defilippi et al., 2016). In addition, to the southwest part of the deposit, stratabound ore bodies composed of pyrrhotite, marcasite and pyrite are emplaced into the Santa Formation. The ore bodies are described for the first time in this study. The Algamarca deposit was dated at 15.5 ± 0.4 Ma by the K-Ar

Table 1
Location and description of samples from the Algamarca deposit.

Sample	Sample type and location	Geographical coordinates	Elevation (m a.s.l.)	Description
RSHA-01	Underground "Dump" Halcon gallery	7° 36′ 15.78″ S, 78° 14′ 33.33″ W	3297	San Blas vein. Quartz with pyrite, chalcopyrite and fahlore. Cut argilized pre mineral intrusive with abundant disseminated pyrite.
RSHA-02	Underground "Dump" Capuli gallery	7° 36′ 21.57″ S, 78° 14′ 37.41″ W	3163	San Blas vein. Massive pyrite with interstitial baryte.
RSHA-03	Underground "Dump" Alisos gallery	7° 36′ 28.41″ S, 78° 14′ 32.99″ W	3131	Alisos vein. Tennantite, chalcopyrite and pyrite with lesser euhedral quartz.
RSHA-04	Underground "Stockpile" Nivel 0 gallery	7° 36′ 26.13″ S, 78° 14′ 37.50″ W	3086	San Blas vein. Chalcopyrite, pyrite, tetrahedrite and euhedral quartz.
RSHA-13	Drill core SH-11–232, from 446.8 to 446.9 m	7° 36′ 36.14″ S, 78° 13′ 12.05″ W	n.a.	Santa Formation. Black shale with disseminated fine-grained pyrite.
RRAL-01A	Underground "In situ" Choloque gallery	7° 36′ 44.11″ S, 78° 13′ 44.44″ W	3261	Chimú Formation. Disseminated euhedral pyrite up to 0.5 cm in sandstone.
RRAL-01B	Underground "In situ" Choloque gallery	7° 36′ 44.11″ S, 78° 13′ 44.44″ W	3261	Choloque vein. Breached texture, clasts of quartzite and matrix of quartz and pyrite (vein width 8 cm).
RRAL-02	Surface outcrop 1 km SE of the veins	7° 37′ 34.10″ S, 78° 13′ 47.22″ W	3318	Santa Formation. Intercalations of siltstone and shale.
RRAL-03	Surface outcrop 1.4 km SE of the veins	7° 37′ 46.65″ S, 78° 13′ 51.42″ W	3352	Santa Formation. Black shale with intercalations of sandstone.
RRAL-04	Surface outcrop 1.4 km SE of the veins	7° 37′ 44.81″ S, 78° 13′ 47.95″ W	3349	Coarse-grained intrusive.
RRAL-05	Underground "In situ" Esperanza gallery	7° 36′ 54.309″ S, 78° 14′ 10.070″ W	3071	Lucy vein. Pyrite-quartz-tennantite- tetrahedrite as matrix and clasts of quartzite from Chimú Formation (vein width 45 cm).
RRAL-06	Underground "In situ" Esperanza gallery	7° 36′ 54.74″ S, 78° 14′ 9.47″ W	3063	Concepción vein. Centimetric hydrothermal quartz crystals with minor pyrite and tennantite- tetrahedrite (vein width 35 cm).
RRAL-07	Underground "In situ" Esperanza gallery	7° 36′ 54.573″ S, 78° 14′ 9.281″ W	3064	Concepción vein. Fine pyrite-quartz veinlets (0.5 cm) cutting the coal beds of Chimú Formation.
RRAL-08	Underground "In situ" Esperanza gallery	7° 36′ 54.518″S, 78° 14′ 9.206″ W	3064	Coal beds of Chimú Formation with disseminated pyrite.
RRAL-09	Underground "In situ" Esperanza gallery	7° 36′ 49.10″ S, 78° 14′ 14.68″ W	3015	Post-mineral intrusive strongly argilized.
RRAL-10	Underground "In situ" Esperanza gallery	7° 36′ 49.08″ S, 78° 14′ 14.66″ W	3015	Iron oxides, chalcocite and covellite in the contact between a vein and post-mineral intrusive.
RRAL-11	Underground "In situ" Esperanza gallery	7° 36′ 45.49″ S, 78° 14′ 28.44″ W	3081	Sill of porphyry quartz diorite intrusive in Santa Formation.
RRAL-12A	Underground "Stockpile" Esperanza gallery	7° 36′ 46.47″ S, 78° 14′ 37.15″ W	3086	Lucy vein. Fahlore, pyrite and quartz with minor chalcopyrite, covellite and chalcocite. Cut by alunite veins.
RRAL-12B	Underground "Stockpile" Esperanza gallery	7° 36′ 46.47″ S, 78° 14′ 37.15″ W	3086	Gangue white minerals (alunite, pyrophyllite, nacrite).
RRAL-13A	Underground "In situ" CX-126 gallery	7° 36′ 56.07″ S, 78° 14′ 43.75″ W	2898	Algamarca ore bodies. Massive pyrrhotite partially replaced by marcasite and pyrite.
RRAL-13B	Underground "In situ" CX-126 gallery	7° 36′ 56.07″ S, 78° 14′ 43.75″ W	2898	Calcite-marcasite veinlets with fine halos of chlorite.
RRAL-014	Underground "In situ" CX-126 gallery	7° 36′ 58.00″ S, 78° 14′ 40.74″ W	2898	Fault with abundant carbonaceous material, minor pyrite and quartz.

m a.s.l. = meters above sea level; n.a. = not available.

method on hydrothermal muscovite found bordering a vein (Noble and McKee,1999). The deposit was classified as intermediate-sulfidation epithermal based on sulfide and gangue mineral assemblages (Defilippi et al., 2016; Galdos et al., 2021). Due to the proximity to the Shahuindo Au-Ag deposit (~1 km; Fig. 1c) and general similarities in ore mineralogy (Vallance et al., 2024), the Algamarca deposit was inferred to be part of the same magmatic-hydrothermal system as Shahuindo (Hodder et al., 2010; Galdos et al., 2021).

2. Samples and methods

2.1. Samples investigated in this study

Samples for this study were collected from underground mining works on the Algamarca veins, drill core, as well as from outcrops surrounding the veins. The San Blas, Alisos, Lucy, Concepción, and Choloque veins were sampled on site, in stockpiles or dumps, depending on underground access authorization. Weathered surfaces were avoided during sampling. In total, 22 samples from 19 different locations were obtained from these veins and their sedimentary and intrusive host rocks (e.g., Fig. A1). Sample locations are identified in Fig. 1c, and their coordinates and brief description are reported in Table 1. A selection of 30 polished sections (2.5 cm in diameter) and 8 doubly-polished thick sections (from 100 to 150 μm thick) were prepared.

2.2. Methods

2.2.1. Optical microscopy and etching

The 30 polished sections from the Algamarca deposit were examined under a reflected-light polarizing microscope to identify the sulfide paragenesis. Based on petrographic descriptions, pyrite crystals were selected for detailed observation to investigate compositional zonation in a single crystal. For that, the polished face of selected sections, containing mainly pyrite, was etched with commercially available bleach solution (4 wt% sodium hypochlorite, NaOCl, in water) for five minutes; then the sections were rinsed under tap cold water and left to dry, following the procedure described by Tanner et al. (2016) and Sykora et al. (2018).

2.2.2. Scanning electron microscopy (SEM) and X-ray powder diffraction (XRD)

Sulfides and gangue minerals were studied using a JEOL JSM 6360LV scanning electron microscope (SEM) equipped with an energy dispersive X-ray spectrometer (EDS) at the GET laboratory, Toulouse, France. Pyrites were observed in backscattered electron mode (BSE) at an acceleration voltage of 20 kV. The BSE images were compared and correlated with images of both pristine and etched pyrite obtained with a conventional optical microscope. X-ray powder diffraction (XRD) analyses of gangue minerals were performed with a Bruker D8 Advance A25 diffractometer at the GET laboratory. The step size was 0.01° and
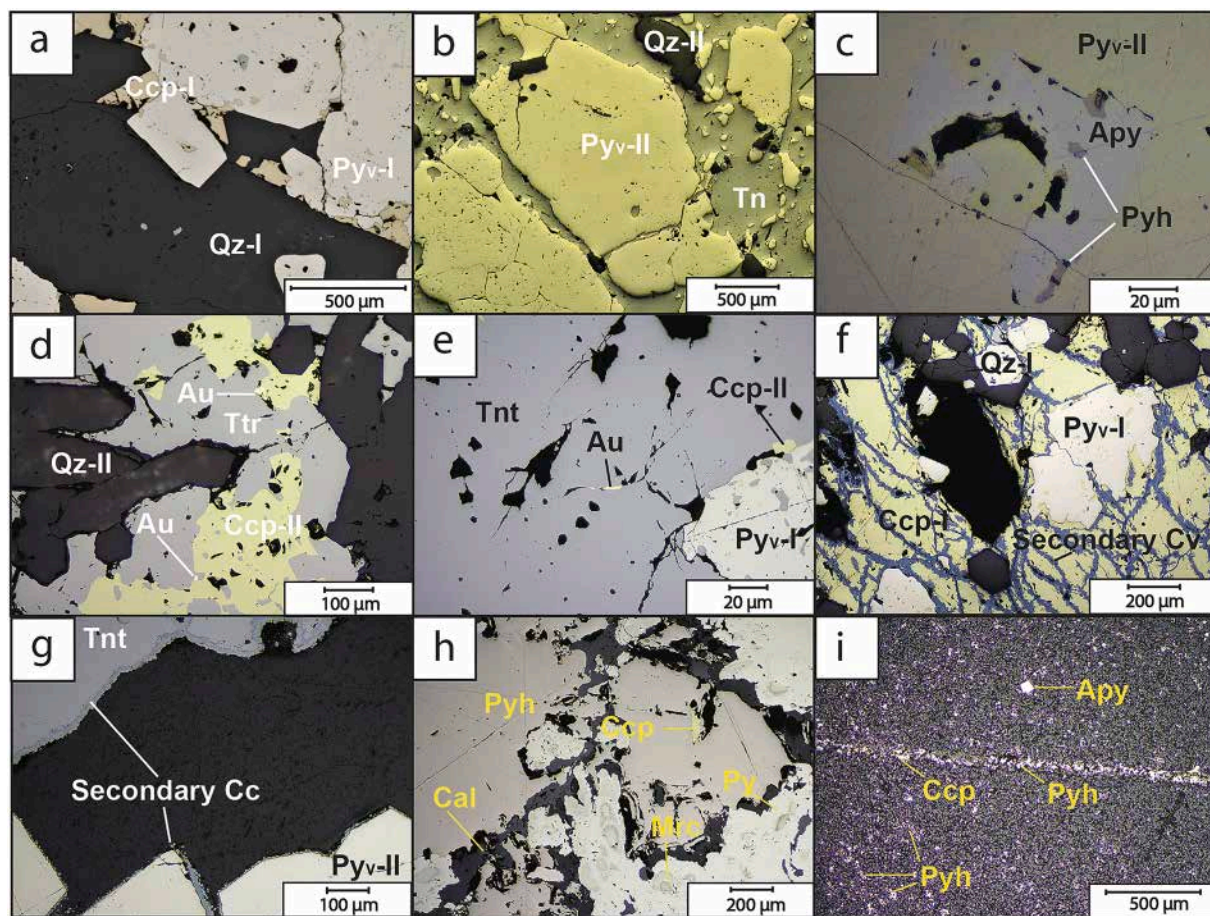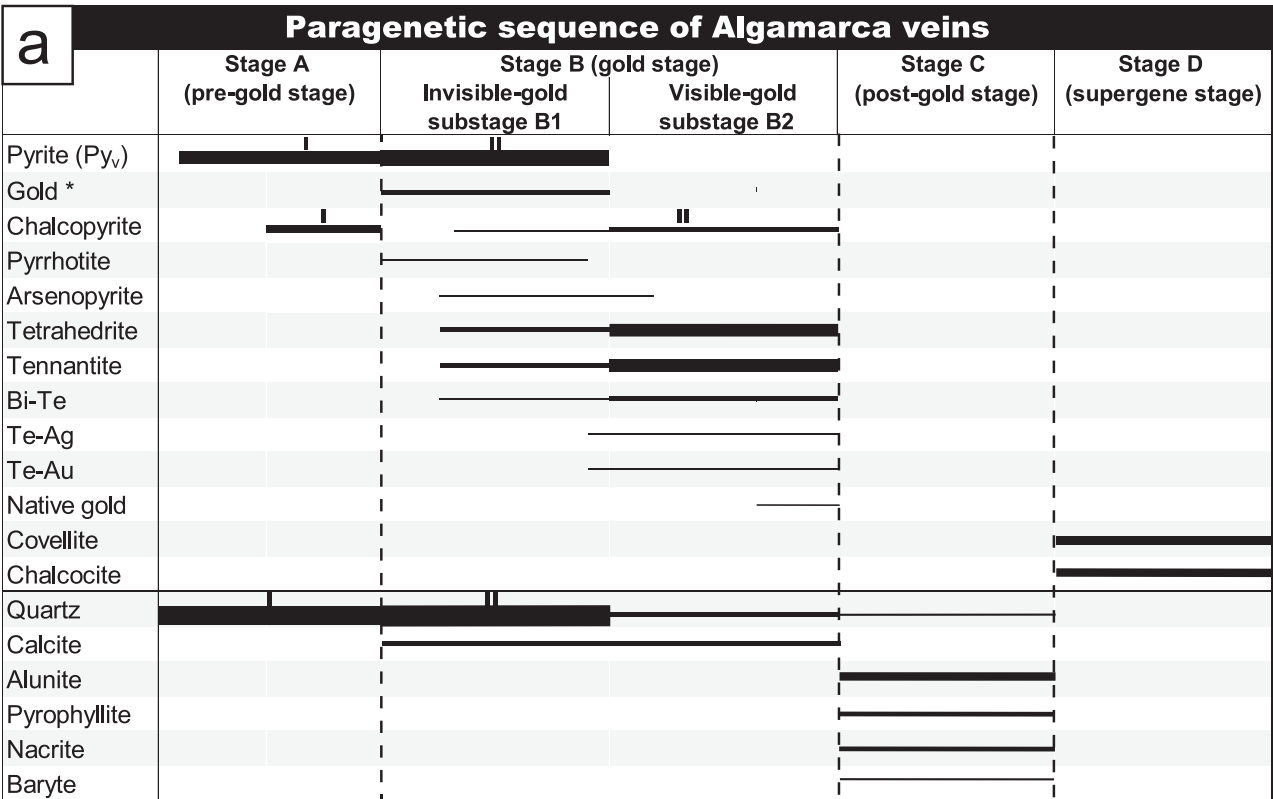

Fig. 3. Photomicrographs in reflected light showing representative textures of ore mineral assemblages in the Algamarca veins (a–g) and ore bodies (h, i). (a) Quartz, pyrite and chalcopyrite from stage A. (b) Tennantite replacing and filling fractures in pyrite. (c) Pyrite including arsenopyrite and pyrrhotite. (d) Native gold at the contact between chalcopyrite and tetrahedrite. (e) Native gold filling microfractures in tennantite. (f) Incipient replacement of chalcopyrite by secondary covellite along fractures and mineral boundaries. (g) Chalcocite replacing tennantite along mineral boundaries and as patina on euhedral pyrite. (h) Marcasite replacing pyrrhotite, partially replaced by pyrite. (i) Disseminated pyrrhotite and arsenopyrite and a narrow vein of pyrrhotite, with local occurrence of chalcopyrite. In all figures, mineral abbreviations follow Warr (2021).

a **Paragenetic sequence of Algamarca veins**

	Stage A (pre-gold stage)	Stage B (gold stage)		Stage C (post-gold stage)	Stage D (supergene stage)
		Invisible-gold substage B1	Visible-gold substage B2		
Pyrite (Py$_v$)					
Gold *					
Chalcopyrite					
Pyrrhotite					
Arsenopyrite					
Tetrahedrite					
Tennantite					
Bi-Te					
Te-Ag					
Te-Au					
Native gold					
Covellite					
Chalcocite					
Quartz					
Calcite					
Alunite					
Pyrophyllite					
Nacrite					
Baryte					

* Invisible-gold in pyrite

b **Paragenetic sequence of Algamarca bodies**

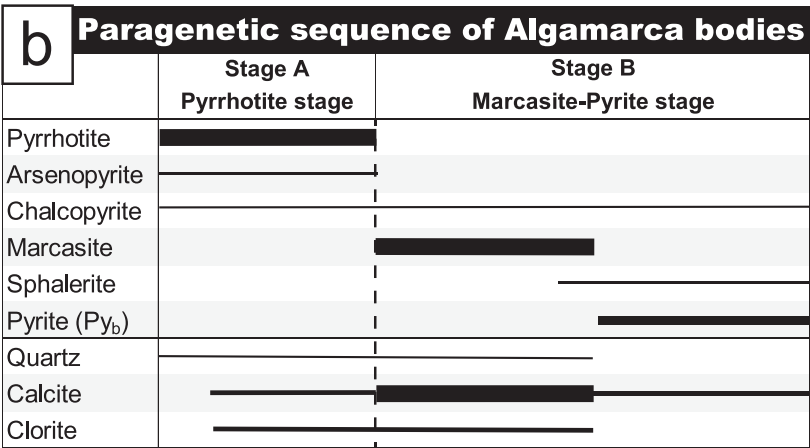|	Stage A Pyrrhotite stage	Stage B Marcasite-Pyrite stage
Pyrrhotite		
Arsenopyrite		
Chalcopyrite		
Marcasite		
Sphalerite		
Pyrite (Py$_b$)		
Quartz		
Calcite		
Clorite		

Fig. 4. Paragenetic sequence of the Algamarca veins (a) and ore bodies (b). Lines thickness is proportional to abundance.

the 2Θ range from 2° to 80°, with an acquisition time of 30 to 60 min per spectrum.

2.2.3. Electron microprobe analyses

Wavelength-dispersive X-ray spectroscopy (WDS) analyses of pyrite, marcasite, pyrrhotite, arsenopyrite, chalcopyrite, tetrahedrite, tennantite and native gold were performed on twelve polished sections with a CAMECA SXFive electron probe micro analyzer (EPMA) at the Raimond Castaing Microanalysis Centre of the University of Toulouse (France) using the following analytical conditions: 25 kV electron gun tension, 20 nA electron current, and 2 μm diameter beam size. The standards were chalcopyrite for S, Fe and Cu; arsenopyrite for As; sphalerite for Zn; and native gold, silver, bismuth and antimony for Au, Ag, Bi and Sb, respectively. The detection limits are reported in Tables A1 and A2.

2.2.4. Laser ablation - inductively coupled plasma mass spectrometry analyses of sulfide minerals

Laser ablation – inductively coupled plasma mass spectrometry (LA-ICPMS) analyses of the same samples and minerals analyzed with EPMA (except native gold) were performed using a Thermo Finnigan HR quadrupole ICP-MS coupled with a UV femtosecond laser at the GET laboratory. The laser ablation was performed under an argon atmosphere and the ablated material was carried by an Ar-He flow from the ablation cell to the spectrometer. Point analyses, a total of 150 datapoints, were obtained with a laser spot size of 25 μm, a pulse frequency of 5 Hz and a 4.5 J.cm^{-2} fluence. Calibrations were performed using Po-726 (Sylvester et al., 2005), MASS-1 (Wilson et al., 2002) and natural arsenopyrite (Pokrovski et al., 2002, 2021) as external standards, and iron as an internal standard whose content was determined by EPMA. Each analysis comprised 30 s of background acquisition and 80 s of
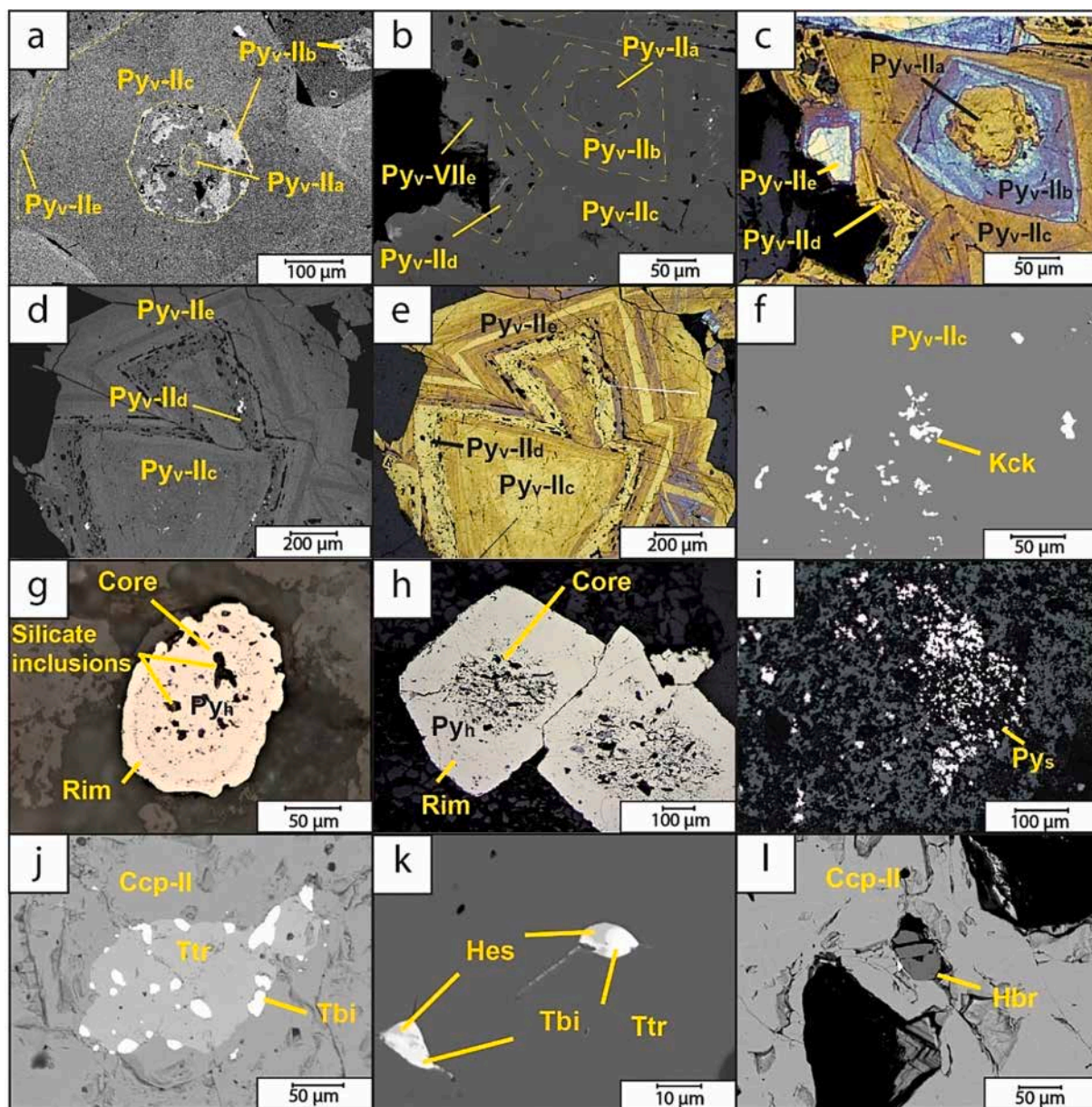
Fig. 5. SEM images in back-scattered electron mode (a, b, d, f, j, k and l), photomicrographs of NaOCl-etched pyrite (c and e) in veins, and photomicrographs in reflected light showing different types of pyrite in the Algamarca deposit (g, h and i). (a) Relicts of Py_v-II_a and Py_v-II_b in Py_v-II_c, Py_v-II_c is rimmed by Py_v-II_e (San Blas vein). (b) Five overgrowth zones of pyrite from stage B (Concepción vein). (c) Etching highlights the contacts between the different overgrowth zones of pyrite from (b). (d) Py_v-II_c, Py_v-II_d and Py_v-II_e (Concepción vein); Py_v-II_d showing cavities parallels to growth bands. (e) Same pyrite crystal as (d) etched with NaOCl. (f) Small crystals of kiddcreekite as inclusions in Py_v-II_c. (g) Hydrothermal pyrite in the intrusive host rock (Py_h) with a porous core with silicate inclusions (host rock relics) and a more compact rim. (h) Hydrothermal pyrite in sedimentary host rock (Py_h), showing a rounded porous core with silicate inclusions rimmed by a massive euhedral growth zone. (i) Anhedral to subhedral synsedimentary to diagenetic disseminated pyrite (Py_s) forming a mosaic of spongy crystals. (j) Association of Bi-Te minerals and tetrahedrite surrounded by chalcopyrite. (k) Small inclusions of telluride in tetrahedrite. (l) Hübnerite embedded in chalcopyrite.

ablation. The following isotopes were measured ^{34}S, ^{33}S, ^{51}V, ^{55}Mn, ^{57}Fe, ^{59}Co, ^{60}Ni, ^{62}Ni ^{63}Cu, ^{65}Cu, ^{66}Zn, ^{68}Zn, ^{69}Ga, ^{75}As, ^{77}Se, ^{82}Se, ^{95}Mo, ^{107}Ag, ^{111}Cd, ^{115}In, ^{118}Sn, ^{121}Sb, ^{125}Te, ^{182}W, ^{197}Au, ^{201}Hg, ^{202}Hg, ^{205}Tl, ^{208}Pb, and ^{209}Bi. Data reduction was carried out using the SILLS software (Guillong et al., 2008).

2.2.5. Raman spectroscopy

Raman spectra of carbonaceous material (CM) and fluid inclusions were acquired at the Centre d'Élaboration de Matériaux et d'Etudes Structurales (CEMES) laboratory in Toulouse, France, using an XploRA PLUS instrument equipped with an Andor CCD detector, and using 1800 lines/mm grating, a confocal hole of 300 μm, and a 532 nm laser passing through a confocal microscope (Olympus, BX51, equipped with a 100x

objective with a numerical aperture of 0.90). Laser power was varied from 0.5 to 10 mW on the sample using optical filters. Acquisition time was 20 s per spectral window for CM and 60 s per window for fluid inclusions, with at least two scans per sample. The data were collected from 100 to 4200 cm^{-1} to cover both first- and second-order C-C and C-H bands wavenumber regions of the CM and the whole range of sulfur, carbon and water vibrations in the fluid inclusions. The spectra were processed using the Fityk program (Wojdyr, 2010). The CM Raman spectra were baseline subtracted and peak fitted following the procedure proposed by Kouketsu et al. (2014), to obtain the following band parameters: peak wavenumber position, intensity, area, and full width at half maximum (FWHM). In these fits, a pseudo-Voigt function (with Gaussian/Lorentzian ratio from 0 to 1) was used for all bands, and the

Table 2

Different types of pyrite present in the Algamarca deposit.

Pyrite type	Origin, location, shape	Size(μm)	Features	Mean concentration	
				EPMA As (wt%)	LA-ICPMS Au (ppm)
Py_s	Synsedimentary/diagenetic, sedimentary host rock, anhedral to subhedral	<20	Distinguished by its fine-grained crystals showing framboidal or spongy texture. Found in the Santa and Chicama formations.	0.2	0.1
Py_v-I	Hydrothermal veins (Stage A), anhedral to subhedral	200–1000	Compact crystals, BSE and etched sample images do not reveal internal textures.	0.4	1.3
Py_v-II	Hydrothermal veins (Stage B), subhedral to euhedral	20–500	Distinguished by its complex texture and zoning in BSE and etched sample images.	0.5	5.1
Py_h	Hydrothermal sedimentary and intrusive host rock, subhedral to euhedral	100–500	Occurring immediately next to the Algamarca veins as disseminated crystals, and displaying a porous core and a compact rim.	0.5	1.4
Py_b	Hydrothermal ore bodies and veinlets, anhedral to euhedral	50–200	Occurring as euhedral grains surrounding marcasite with bird's eye texture in ore bodies, and in calcite-marcasite-pyrite veinlets.	b.d.l.	b.d.l.

b.d.l. = below detection limit.

position of so-called G-band was fixed at 1593 cm^{-1} (Kouketsu et al., 2014).

2.2.6. Fluid inclusion petrography, microthermometry, and LA-ICPMS analyses

Quartz from the Algamarca veins contains a plethora of fluid inclusions that were investigated as detailed below. Prior to analyses, careful fluid inclusion petrography was carried out using a petrographic microscope, assisted by scanning electron microscopy-cathodoluminescence (SEM-CL), in order to distinguish different generations in the quartz host. SEM-CL images were acquired at the GET laboratory, using a TESCAN VEGA S5122 equipped with a Rainbow CL detector. The acceleration voltage and current applied were 10 kV and 10 nA, respectively. Microthermometry measurements were carried out at the GET laboratory on seven doubly polished sections (about 150 μm thick), using a Linkam THMSG-600 heating-freezing stage mounted on a BX51 Olympus microscope. The temperature was calibrated using the ice melting temperature (Tm_{ice}) and the homogenization temperature (Th) of pure H_2O synthetic fluid inclusions at 220 bar (0 and 374.1 °C) and the melting temperature of solid CO_2 (Tm_{CO2}) of pure CO_2-bearing inclusions from Camperio (–56.6 °C). The accuracy of temperature measurements on the calibrators was ±0.2 °C (at –56.6 and 0 °C) and ±2 °C (at 374.1 °C). The measurements were conducted on fluid inclusion assemblages (FIAs), i.e. groups of synchronously trapped inclusions with a similar phase ratio, according to the criteria defined by Goldstein and Reynolds (1994). The salinity was estimated from i) the ice melting temperature (Tm_{ice}) according to the equation of Bodnar (1993) in liquid-rich and vapor-rich fluid inclusions; ii) the halite dissolution temperature (Tm_{hal}) following the equation of Potter and Brown (1977) in multiphase-solid fluid inclusions. Pressure values were estimated from the equations of Zhang and Frantz (1987) and Bodnar and Vityk (1994) for the PVTX properties of water-salt-gas systems, using the Loner38 and Fluids software, respectively (Bakker, 2003).

Individual element concentrations of single fluid inclusions were analyzed using a COMPex nanosecond excimer laser coupled to an Agilent 8900 triple quadrupole ICP mass spectrometer at the University of Geneva. The beam diameter was varied from 15 to 65 μm in order to ensure complete ablation of the fluid inclusion depending on its size while minimizing the addition of the host to the signal. The analyzed isotopes for all fluid inclusions were ^{11}B, ^{23}Na, ^{25}Mg, ^{34}S, ^{35}Cl, ^{39}K, ^{44}Ca, ^{55}Mn, ^{57}Fe, ^{65}Cu, ^{66}Zn, ^{75}As, ^{88}Sr, ^{107}Ag, ^{121}Sb, ^{133}Cs, ^{197}Au, and ^{208}Pb, with addition of ^{79}Br, ^{85}Rb, ^{95}Mo, ^{137}Ba, and ^{209}Bi for multiphase-solid fluid inclusions. A dwell time of 10 ms was used for all elements except Au (40 ms), S, Cl and Ag (30 ms), Mo (20 ms), and Si (5 ms). Calibrations were performed using the NIST glass standard SR-610 (Norman et al., 1996) and an in-house andesitic glass standard doped with Cl and S (for chlorine and sulfur) as external calibrators, and the Na concentration in

the fluid inclusion as an internal standard. This concentration was assessed from the bulk salinity (wt % NaCl eq.) calculated from the ice melting and halite dissolution temperatures and corrected for the presence of the other major salts such as KCl, $CaCl_2$, $FeCl_2$, $MnCl_2$ from the LA-ICPMS analyses of the corresponding metal cations and using an iterative algorithm of Heinrich et al. (2003) implemented in the SILLS software (Guillong et al., 2008). For the quartz host, SiO_2 was used as internal standard, assuming nearly pure quartz (99.99 % SiO_2).

3. Results

3.1. Mineralogy, pyrite types and paragenetic sequence

3.1.1. Algamarca veins

Most Algamarca veins display crustiform, colloform and breccia textures, which are typical textures of open space precipitation (Fig. A1a-d; Echavarria et al., 2006). Most veins consist essentially of quartz (~40 %), pyrite (~30 %), tetrahedrite-tennantite (~10 %), and chalcopyrite (~10 %; Fig. A1c-h), the latter being much less abundant (<2%) in the Lucy, Concepción, and Choloque veins located southeast of the deposit. Pyrite occurring in the veins is hereafter termed (Py_v). The sulfides listed above, along with secondary chalcocite and covellite, are the only phases visible at the macroscopic scale (by naked eye or with the help of a hand lens). The veins also contain minor arsenopyrite (FeAsS), Bi-Te alloys, galena (PbS), sphalerite (ZnS), pyrrhotite ($Fe_{1-x}S$), hübnerite ($MnWO_4$), tungstenite (WS_2), kiddcreekite (Cu_6SnWS_8), stannite (Cu_2FeSnS_4), Ag and Au tellurides, and native gold (e.g., Fig. 3c-e), which were detected using an optical microscope or SEM. Calcite, alunite, nacrite, pyrophyllite, and baryte are minor gangue phases. Based on crosscutting relationships and replacement textures identified in the field, hand samples, and observations under the microscope, the following paragenetic sequence with four stages (A, B, C, and D) has been established (Fig. 4a).

Stage A (pre-gold stage). The assemblage consists of quartz (Qz-I), pyrite (Py_v-I) and chalcopyrite (Ccp-I; Fig. 3a). These minerals mainly occur as clasts in a matrix of minerals from later stages. Py_v-I presents a simple texture, without overgrowth zones, and etching and SEM images did not reveal any internal textures. The pyrite has subangular to subrounded edges, 0.1–5.0 mm size. Stage A was only identified in the Descubridora, San Blas, and Alisos veins.

Stage B (gold stage). Stage B represents the main event of gold mineralization in Algamarca veins. At this stage, it is common to see breached textures, where the clasts are fragments of the host rock (quartzite of the Chimú Formation; Fig. A1c, d) and/or minerals from stage A. This stage can be divided in two substages, B1 and B2. An invisible gold substage, B1, is characterized by an arsenic-rich pyrite hosting invisible-gold (labelled as Py_v-II), accompanied by euhedral
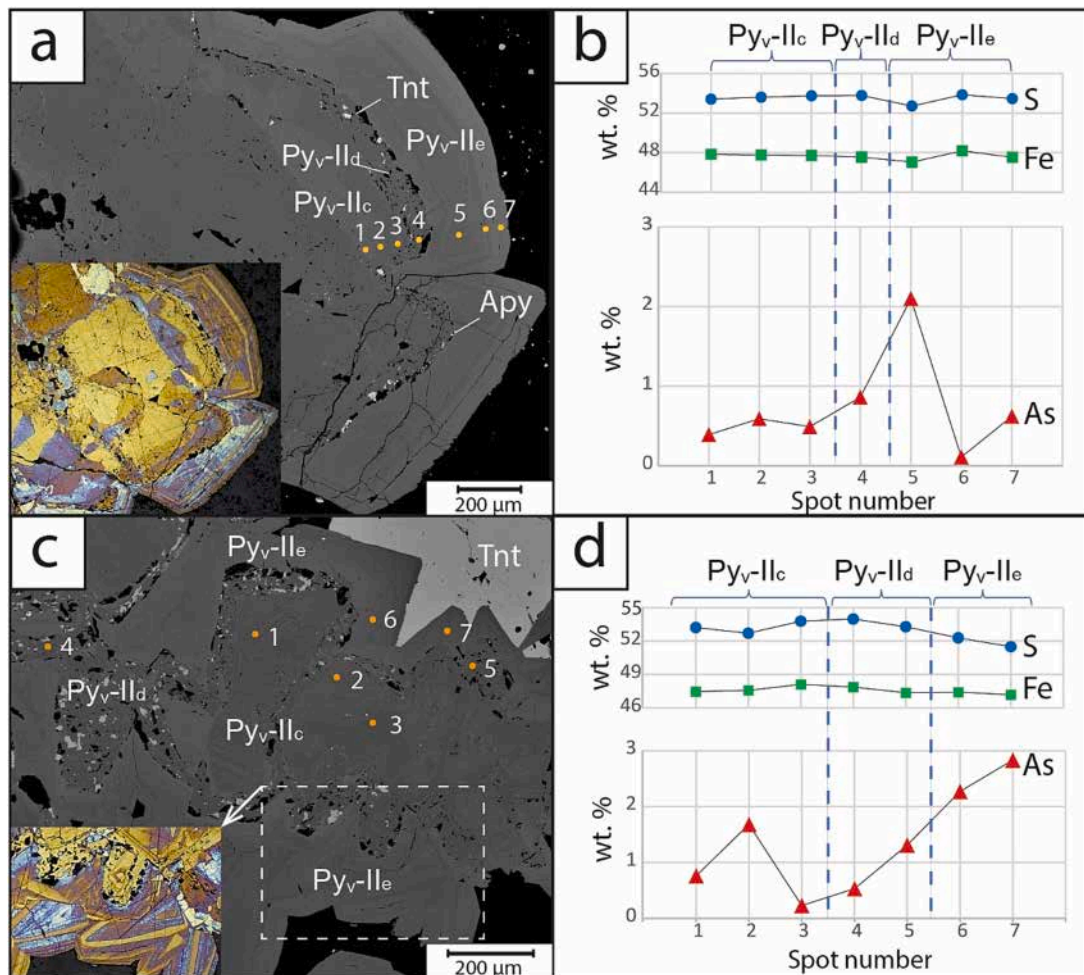
Fig. 6. Back scattered electron images of Py_v-II from the Lucy vein (a and c). Py_v-II$_d$ overgrowing Py_v-II$_c$ and showing porosity and abundant inclusions of arsenopyrite (Apy) and tennantite (Tnt). Euhedral Py_v-II$_e$ overgrowing Py_v-II$_d$ and presenting distinctive oscillatory zoning. The images of NaOCl-etched pyrite on the lower-left corners highlight high arsenic content in blue and white tints. (b and d) Concentration of S, Fe and As, obtained from EPMA analysis; analytical spots are located by orange dots in (a) and (c).
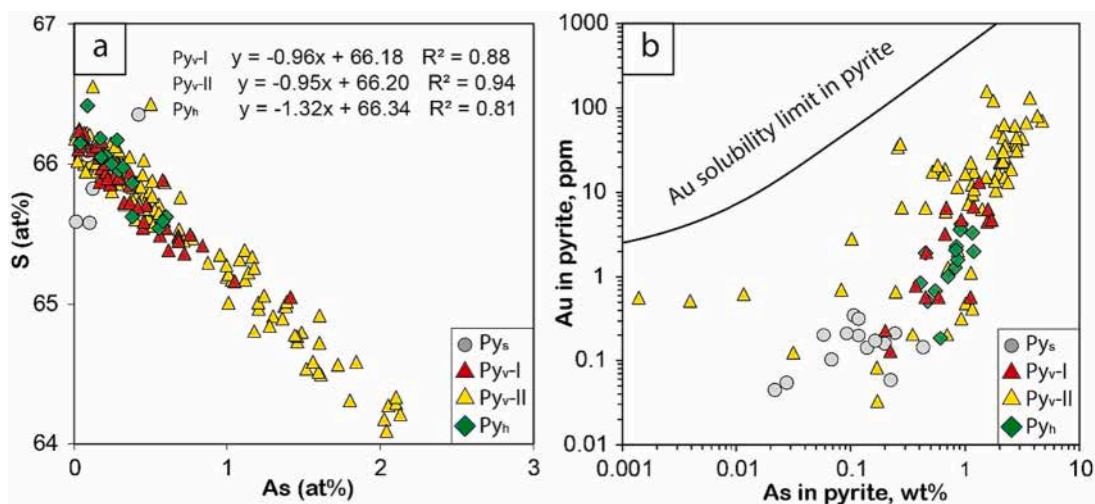

Fig. 7. EPMA (a) and LA-ICPMS (b) data on pyrites from the Algamarca deposit. (a) Distribution of As vs. S. (b) Au-As log–log plot. Abbreviations for pyrites types are from Table 2. The black curve of Au solubility limit is according to Reich et al. (2005).
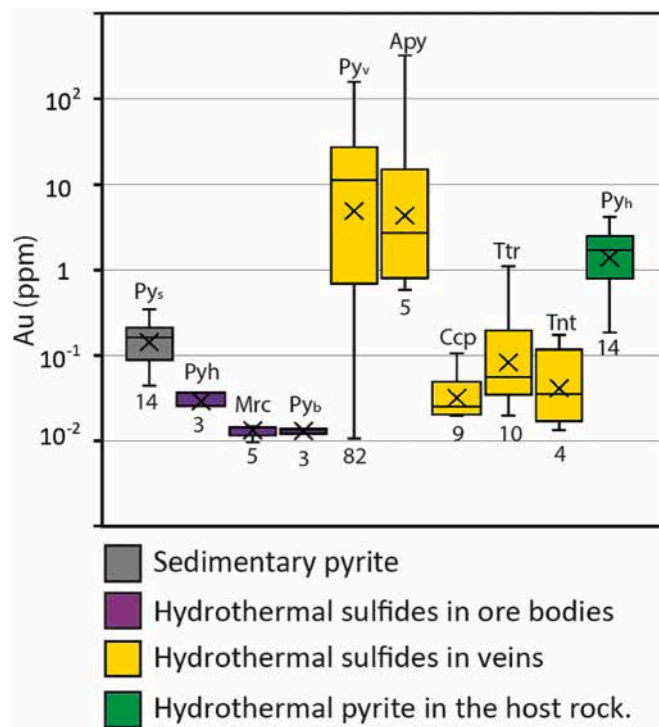
Fig. 8. Box plot comparing Au concentrations (in ppm) in different sulfides from the Algamarca deposit. Values below detection limit (DL, 0.03–0.05 ppm Au, depending on the mineral) are shown as half their DL value. Crosses denote the geometric mean. The host sulfide and the number of analyses are indicated, respectively, above and below each box. Pyrites are labelled as in Table 2.

quartz (Qz-II). A visible-gold substage, B2, is characterized by the ubiquitous presence of up to 30 μm native gold microparticles, commonly found as inclusions and filling microfractures in tetrahedrite-tennantite crystals, or at the boundary between this mineral and chalcopyrite (Fig. 3d, e). Both sub-stages are described in more detail as follows.

Substage B1 – invisible-gold mineralization – is characterized by the following features. The ore mineral is the arsenian pyrite, i.e. Py_v-II, which is characterized by several overgrowth zones (Fig. 5a-e). In a single Py_v-II crystal, we have been able to identify up to five distinct pyrite zones (labelled as "a" to "e") by clear cross-cutting relationships, which likely indicate the different precipitation steps during the invisible-gold substage. These overgrown zones are distinguished as follows. i) Py_v-II_a has irregular boundaries due to corrosion, and it is dark in BSE images and yellow to orange in etched sample images (Fig. 5a-c). ii) Py_v-II_b is euhedral and usually shows sharp contacts with earlier and later generations, it is bright in BSE images and blue after being etched (Fig. 5a-c). iii) Py_v-II_c is the most abundant and is crosscut or overgrown by Py_v-II_d and/or Py_v-II_e, it is dark to bright in BSE images and yellow to orange in etched sample images (Fig. 5a-e). The Py_v-II_c type occasionally contains inclusions of galena, sphalerite, chalcopyrite, stannite and kiddcreekite (e.g., Fig. 5f). iv) Py_v-II_d is porous, and its pores are elongated and parallel to the growth bands. Py_v-II_d is dark in BSE images and yellow to orange in etched sample images (Fig. 5c-e). Py_v-II_d overgrowth zones present abundant anhedral inclusions of arsenopyrite, tetrahedrite-tennantite, chalcopyrite, and pyrrhotite. v) Py_v-II_e, is euhedral in form and shows an oscillatory zoning. It is mainly found overgrowing to Py_v-II_d or Py_v-II_c (Fig. 5a-e and 6a, c). It also occurs as tiny crystals of less than 200 μm in size. This pyrite type also hosts scarce inclusions of arsenopyrite, pyrrhotite and chalcopyrite (Fig. 3c). Py_v-II_e is dark to bright in BSE images and yellow to orange to blue in etched samples (Fig. 5a-e); these variations are due to differences in As content in the lattice of Py_v-II_e. The identified overgrowth types in

pyrite are associated with successive crystallization events, in which earlier precipitated cores were corroded, replaced, or overgrown by a successive pyrite. These zones are interpreted as dissolution-reprecipitation textures and are typically exhibited by pyrite in ore deposits (e.g., Sykora et al., 2018; Wu et al., 2019; Ishida et al., 2021). In the invisible-gold substage (B1), pyrite also is found as disseminated grains in the sedimentary and intrusive host rocks that surround the veins (Fig. 5g, h). These pyrite crystals (labelled as Py_h) present a porous core, containing relicts of the host rock as inclusions and overgrown by more compact rims without pores (Fig. 5g, h). This Py_h type is easily distinguishable from the regionally distributed *syn*-sedimentary or diagenetic pyrite (Py_s), as it is characterized by framboidal or spongy textures and does not display overgrowths (Fig. 5i). The main characteristics of the different types of pyrite present in the Algamarca deposit are reported in Table 2, and their position in the sedimentary sequence is represented in Fig. 2.

Substage B2 – visible-gold mineralization – is distinguished by the following features. Tetrahedrite and tennantite are the most abundant sulfides to have precipitated during this mineralization event, accompanied by minor chalcopyrite (Ccp-II). Tetrahedrite, tennantite and chalcopyrite locally fill (micro)fractures in Qz-II and Py_v-II from the invisible-gold substage (Fig. 3b). Bismuth-bearing minerals (e.g., tellurobismuthite) are common; they occur as anhedral inclusions in tetrahedrite-tennantite and as minor phases associated with chalcopyrite (Fig. 5j). Bismuth-bearing minerals inclusions are spatially associated with silver and gold telluride inclusions (Fig. 5k). Arsenopyrite occurs as euhedral crystals of less than 20 μm, or as larger anhedral crystals (up to 200 μm) partly replaced by tennantite-tetrahedrite and chalcopyrite. Tungsten and tin minerals (e.g., kiddcreekite, Kck and hübnerite, Hbr) are present as inclusions in pyrite, chalcopyrite, tennantite, and tennantite (e.g., Fig. 5f, l).

Stage C (post-gold stage). Stage C is recognized by the presence of nacrite, pyrophyllite, alunite, and baryte (Fig. A1b), which were identified by XRD analyses (Fig. A2). These minerals fill reopened veins or form veinlets that crosscut all previous stages (Fig. A1h). Stage C was recognized in the Concepción, Lucy, and San Blas veins.

Stage D (supergene stage). The last stage, termed D, reflects supergene processes occurring after the deposit formation. It is clearly seen near the surface where the sulfides from stages A and B are replaced by goethite and hematite (Fig. A1d). In deeper parts, secondary Cu-bearing sulfides (chalcocite and covellite) replace chalcopyrite, tetrahedrite, and tennantite (Fig. 3f, g). Chalcocite is also found as a patina on pyrite (Fig. 3g).

3.1.2. Ore bodies

In addition to the veins described above, several <10 cm thick stratabound ore bodies replace carbonate beds in the Santa Formation. This type of mineralization was only observed in the CX-126 gallery and, as far as we know, has not been reported before in the Algamarca deposit. The ore bodies consist of massive pyrrhotite (stage A), crosscut and replaced by marcasite (Fig. A1j), which is subsequently replaced by pyrite (stage B; Fig. 3h). Pyrite in the ore bodies is hereafter referred to as Py_b. Minor chalcopyrite (stages A and B) and sphalerite (stage B) are also present. The rock immediately next to the orebodies is strongly chloritized and two types of veinlets are present: veinlets < 0.5 cm wide consisting of pyrrhotite and scarce chalcopyrite, corresponding to stage A (Fig. 3i), and veinlets up to 2 cm wide bearing calcite, marcasite, and minor pyrite (Py_b) with a narrow chlorite halo (Fig. A1k), corresponding to stage B. Euhedral to subhedral quartz crystals up to 0.7 mm in size occur in association with chlorite, both in ore bodies and veinlets. Fine disseminations of pyrrhotite with sporadic crystals of arsenopyrite (up to 100 μm) appear next to the ore bodies and pyrrhotite veinlets (Fig. 3i). The paragenetic sequence of Algamarca ore bodies is shown in Fig. 4b.
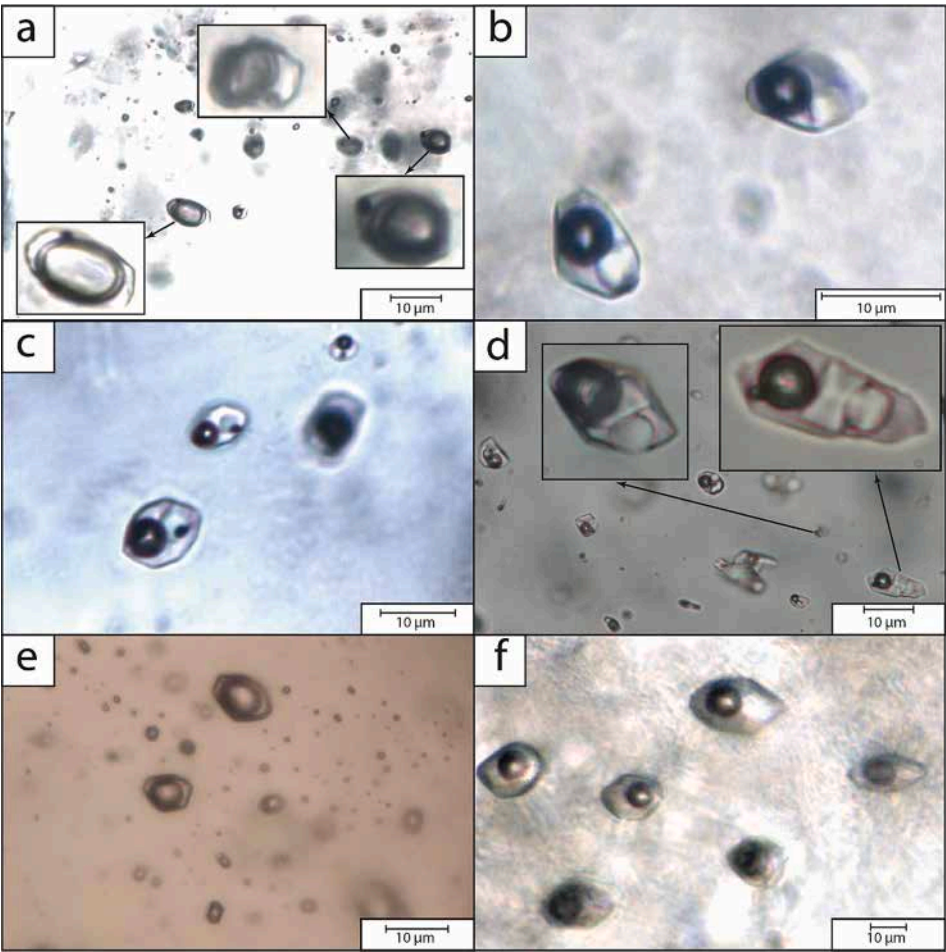
Fig. 9. Photomicrographs of fluid inclusions and fluid inclusion assemblages (FIAs) in quartz from stage A (Qz-I; a-e) and stage B (Qz-II; f), from the San Blas and Concepción veins. (a) An immiscible-liquid (four-phase) FIA along a healed fracture. (b) A multiphase solid (three-phase) FIA. (c) A multiphase solid (four-phase) FIA. (d) Close-up of two fluid inclusions from a multiphase solid (five-phase) FIA. (e) A vapor-rich (two-phase) FIA. (f) A liquid-rich (two-phase) FIA.
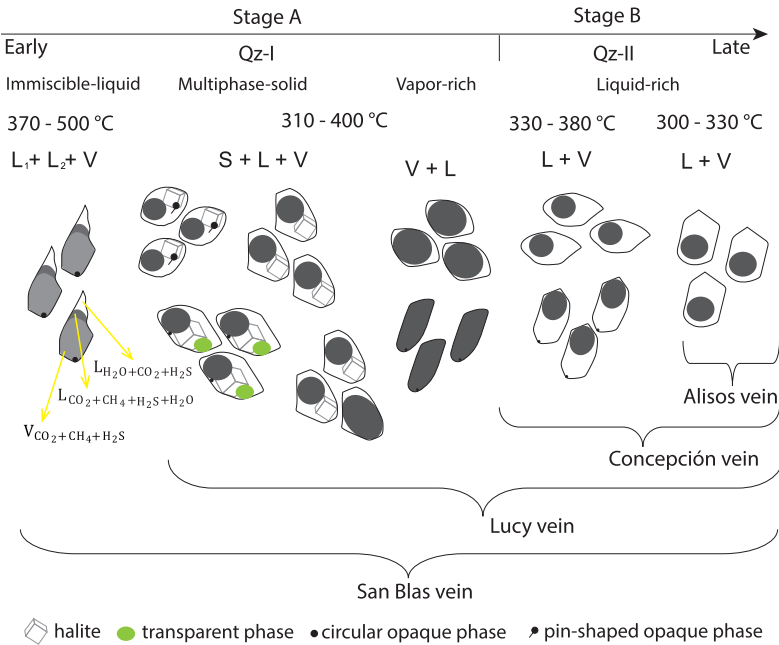

Fig. 10. Schematic representation of the different types of fluid inclusions identified in quartz from the Algamarca veins. The sketches respect the actual shapes of fluid inclusions and the proportions among the different phases.
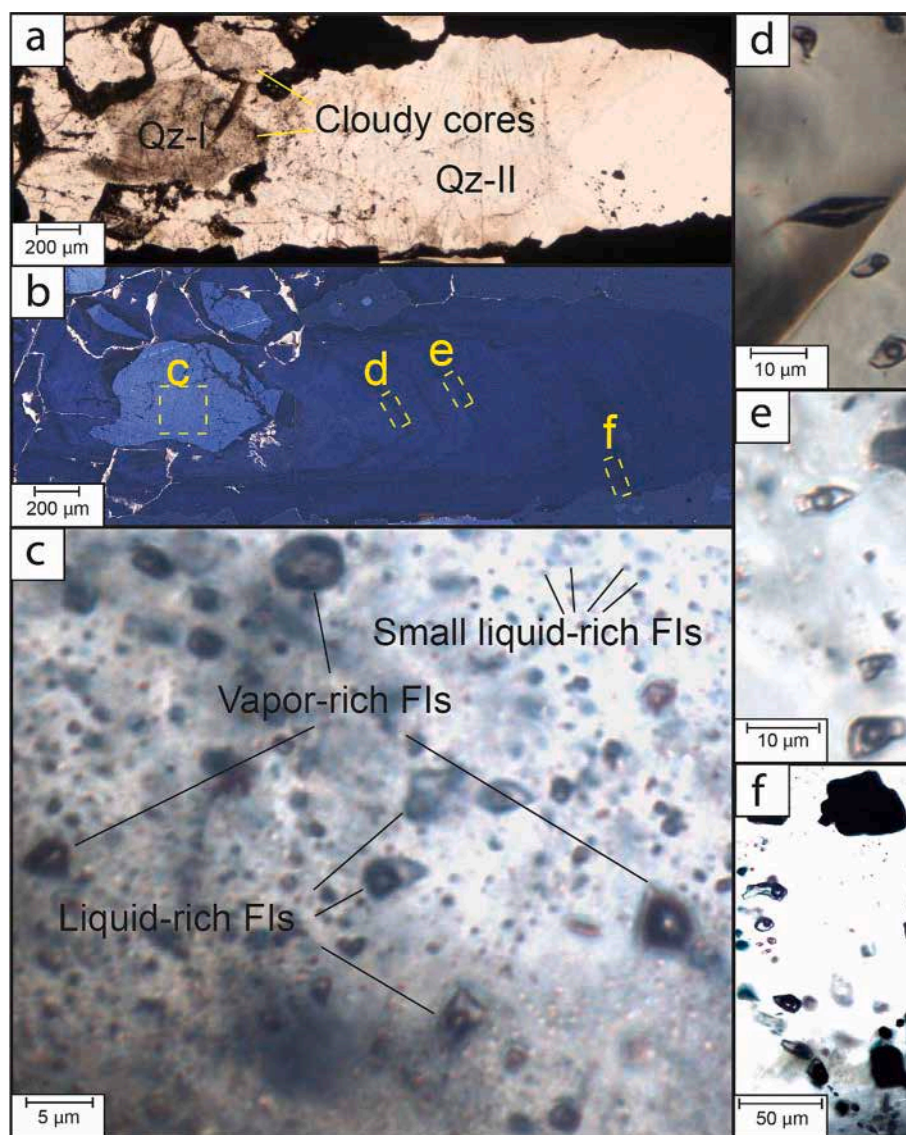
Fig. 11. (a) Transmitted-light photomicrograph of a quartz crystal from the Lucy vein. (b) Scanning electron microscopy-cathodoluminescence (SEM-CL) image of the same crystal from (a), with highly luminescent cloudy cores (Qz-I). Yellow rectangles locate the images in (c–f). (c) Cloudy cores consist of abundant randomly distributed liquid-rich, vapor-rich and multiphase-solid fluid inclusions, mostly smaller than 2 μm. (d) Fluid inclusions from a primary liquid-rich FIA hosted in a growth zone in quartz. (e) Detail of a primary liquid-rich FIA in a growth zone in quartz. (f) Detail of a pseudosecondary liquid-rich FIA in quartz.

3.2. Pyrite composition

3.2.1. EPMA major element analyses

The major-element content of pyrite ranges from 50.7 to 54.0 wt% for S (i.e. from 64.1 to 66.5 at%) and from 46.0 to 48.2 wt% for Fe (i.e. from 33.1 to 34.4 at%). Except As, Cu, and Sb, all other trace element concentrations in pyrite are below the detection limit (Sb was only detected in one point at 0.04 wt%). Copper was detected in <25 % of the points, at values of <0.1 wt% (except one point at 0.2 wt%). The As content in pyrite is variable, ranging from the detection limit (<0.06 wt%) to 4 wt% (Figs. 6, 7a, A5; Tables 2, A1, A2). Sedimentary pyrite (Py$_s$) shows up to 0.3 wt% As (with one point at 0.8 wt%), with half of the datapoints being below the detection limit (<0.06 wt%). The hydrothermal pyrite disseminated in the host rock (Py$_h$) presents moderate As concentrations (Fig. 7a), with cores from 0.1 to 0.4 wt%, and rims between 0.3 and 1.1 wt% As (Table A1). Hydrothermal pyrite in veins (Py$_v$) generally displays the highest values (up to 4.0 wt% in stage B, and up to 2.6 wt% in stage A; Fig. 7a; Table A1), but As concentration variations are substantial depending on the zones. Py$_v$-II$_a$ shows low As

concentrations, <0.3 wt%, while Py$_v$-II$_b$ shows consistently higher As contents, between 2.1 and 3.9 wt%. In the later pyrite zones, the As content is variable. Py$_v$-II$_e$ exhibits the strongest variations due to its oscillatory zoning between bands with As contents below detection limit (yellow in etched pyrite and dark in BSE image) and bands with up to 3.0 wt% As (red and blue in etched pyrite and bright in BSE image; Fig. 6a-d). The As content in hydrothermal pyrites from veins and disseminated in the sedimentary host rock (Py$_v$ and Py$_h$) shows a clearly negative correlation with S, with slope values close to 1 (in at %) indicating a stoichiometric substitution of As for S in the pyrite structure (Fig. 7a). In contrast, pyrite from orebodies (Py$_b$) displays As concentrations below the detection limit (<0.06 wt%).

3.2.2. LA-ICPMS trace element analyses

Pyrite is the most ubiquitous sulfide mineral in the Algamarca deposit. LA-ICPMS in situ analyses were performed on the different pyrite types recognized in the deposit. Crystals containing too many inclusions, or exhibiting strong porosity and/or fracture density, were carefully avoided. Most of the analyses were performed on hydrothermal pyrite

Table 3

Results of microthermometry from fluid inclusion assemblages (FIAs) in quartz from the Algamarca veins and orebodies. For each parameter, the average values are given; the number of analyzed fluid inclusions is in brackets.

Sample	Inclusion appearance	Daughter mineral	Th (°C)	Nb pts	Tm$_{(ice)}$ or Tm$_{(hal)}$ (°C)	Nb pts	wt% NaCl eq.	Density (g/cm^3)[1]	Minimum pressure (bars)[2]
					Ore bodies, liquid-rich type				
RRAL-13	C	—	270 ± 8	(5)	−10.8 ± 0.7	(4)	14.8 ± 0.7	0.92 ± 0.01	48 ± 8
RRAL-13	I	—	247	(1)	−9.4	(1)	13.3	0.93	34
RRAL-13	PS	—	289	(1)	−12.3 ± 0.5	(2)	16.4 ± 0.5	0.91	69
					Lucy vein, liquid-rich type				
RRAL-05	C	—	309 ± 1	(5)	−3.4 ± 0.5	(2)	5.6 ± 0.7	0.76 ± 0.01	92 ± <1
RRAL-05	P	—	311 ± 5	(3)	−2.8 ± 0.5	(3)	4.7 ± 0.7	0.74 ± <0.01	96 ± 7
RRAL-05	P	—	321 ± 10	(3)	−2.3 ± 0.2	(3)	3.9 ± 0.4	0.7 ± 0.02	111 ± 15
RRAL-05	PS	—	308 ± 5	(2)	−5.0 ± 0.4	(3)	7.9 ± 0.6	0.8 ± 0.01	87 ± 6
RRAL-05	C	—	308 ± 8	(4)	−5.0 ± 0.5	(3)	7.9 ± 0.6	0.8 ± 0.02	88 ± 7
RRAL-05	PS	—	299 ± 3	(4)	−6.0 ± 0.4	(4)	9.2 ± 0.5	0.82 ± 0.01	81 ± 4
RRAL-05	C	—	302	(1)	−11.5 ± 0.5	(2)	15.4 ± 0.5	0.89	84
RRAL-05	RD	—	349 ± 15	(9)	−5.1 ± 0.5	(3)	8.0 ± 0.7	0.74 ± 0.02	140 ± 40
RRAL-05	RD	—	329 ± 11	(3)	−10.1 ± 1.7	(3)	14.0 ± 1.8	0.84 ± 0.04	121 ± 17
RRAL-05	RD	—	352 ± 22	(2)	−5.4 ± 0.3	(2)	8.4 ± 0.4	0.72 ± 0.05	164 ± 42
					Alisos vein, liquid-rich type				
RSHA-03	P	—	307 ± 3	(7)	−2.5 ± 0.6	(5)	4.2 ± 0.9	0.74 ± 0.01	89 ± 3
RSHA-03	C	—	316 ± 6	(6)	−2.2 ± 0.4	(4)	3.7 ± 0.7	0.71 ± 0.02	103 ± 10
RSHA-03	I	—	314 ± 4	(2)	−1.9 ± 0.4	(2)	3.2 ± 0.7	0.71 ± <0.01	100 ± 6
RSHA-03	P	—	321 ± 4	(2)	−3.0 ± 1.3	(2)	5 ± 2.1	0.72 ± 0.04	110 ± 5
RSHA-03	P	—	323 ± 2	(3)	−3.5	(1)	5.7	0.73	114
					Concepción vein, liquid-rich type				
RSHA-06	C	—	295 ± 1	(6)	−3.2 ± 0.3	(6)	5.3 ± 0.5	0.78 ± 0.01	76 ± 2
RSHA-06	C	—	298 ± 3	(3)	−3.1 ± 0.1	(2)	5.1 ± 0.1	0.77	77
RSHA-06	I	—	273 ± 2	(2)	−2.5 ± 0.2	(2)	4.1 ± 0.3	0.8 ± 0.01	56 ± 2
RSHA-06	PS	—	280 ± 5	(3)	−4.5 ± 0.2	(3)	7.2 ± 0.2	0.83 ± 0.01	60 ± 4
RSHA-06	P	—	377 ± 1	(3)	−3.1 ± 0.3	(3)	5.1 ± 0.5	0.6 ± 0.01	213 ± 2
RSHA-06	P	—	345 ± 3	(5)	−3.8 ± 0.3	(3)	6.2 ± 0.5	0.7 ± 0.02	146 ± 4
RSHA-06	C	—	288 ± 2	(3)	−2.3 ± 0.4	(2)	3.9 ± 0.6	0.77 ± 0.01	67 ± 3
RSHA-06	P	op	371 ± 14	(3)	−4.1 ± 0.3	(4)	6.6 ± 0.5	0.64 ± 0.04	202 ± 30
RSHA-06	C	—	289 ± 1	(5)	−4.1 ± 0.2	(3)	6.6 ± 0.2	0.8 ± 0.01	69 ± 1
RSHA-06	I	—	283	(1)	−3.0	(1)	5.0	0.79	63
RSHA-06	C	—	281 ± 7	(2)	−2.5 ± 1.0	(2)	4.2 ± 2.0	0.79 ± 0.04	61 ± 7
RSHA-06	I	—	312 ± 3	(2)	−1.8 ± 0.3	(2)	3.1 ± 0.5	0.71 ± 0.01	97 ± 4
RSHA-06	I	—	311 ± 1	(2)	−1.5 ± 0.1	(2)	2.6 ± 0.1	0.71 ± 0.01	96 ± 1
RSHA-06	C	—	283 ± 2	(3)	−3.6 ± 1.0	(3)	5.9 ± 1.4	0.81 ± 0.02	63 ± 2
RSHA-06	C	op	351 ± 2	(7)	−3.7 ± 0.3	(7)	6.0± 0.4	0.67 ± 0.01	160 ± 3
RSHA-06	C	—	290 ± 9	(3)	−3.5 ± 0.1	(3)	5.7 ± 0.2	0.79 ± 0.02	70 ± 10
RSHA-06	C	—	256 ± 9	(3)	−7.1 ± 0.3	(3)	10.6 ± 0.3	0.89 ± 0.01	40 ± 6
RRAL-06_2	C	op	348 ± 2	(6)	−1.9 ± 0.1	(6)	3.2 ± 0.1	0.63 ± 0.01	154 ± 3
RRAL-06_2	C	op	349 ± 1	(7)	−3.6 ± 0.1	(7)	5.9 ± 0.1	0.68 ± 0.01	156 ± 1
RRAL-06_2	P	op	357 ± 1	(13)	−3.3 ± 0.1	(13)	5.4 ± 0.2	0.65 ± 0.01	171 ± 1
RRAL-06_2	P	—	358 ± 6	(4)	−2.5 ± 0.1	(4)	4.2 ± 0.2	0.63 ± 0.02	174 ± 13
RRAL-06_2	C	op	291 ± 1	(6)	−3.1 ± 0.1	(6)	5.2 ± 0.1	0.79 ± 0.01	71 ± 2
RRAL-06_2	PS	—	360 ± 1	(7)	−3.6 ± 0.1	(6)	5.8 ± 0.2	0.65 ± 0.01	177 ± 3
RRAL-06_2	PS	—	365 ± 3	(6)	−7.4 ± 0.1	(6)	11 ± 0.2	0.74 ± 0.01	187 ± 6
RRAL-06_2	P	—	308 ± 2	(4)	−6.6 ± 1.0	(2)	9.9 ± 2.0	0.82 ± 0.01	91 ± 2
RRAL-06_2	P	—	308 ± 1	(4)	−6.2 ± 0.2	(4)	9.4 ± 0.2	0.81 ± 0.01	91 ± 1
RRAL-06_2	P	—	309 ± 1	(4)	−6.0 ± 0.1	(4)	9.1 ± 0.1	0.81 ± 0.01	93 ± 1
RRAL-06_2	P	—	307 ± 3	(7)	−6.2 ± 0.2	(6)	9.4 ± 0.3	0.81 ± 0.01	89 ± 2
RRAL-06_2	P	—	305 ± 1	(4)	−6.7 ± 0.1	(4)	10.0 ± 0.2	0.82 ± 0.01	88 ± 1
RRAL-06_2	C	—	299 ± 9	(4)	−10.5 ± 0.1	(4)	14.4 ± 0.1	0.88 ± 0.01	82 ± 11
RRAL-06_2	PS	—	378 ± 1	(8)	−2.8 ± 0.1	(7)	4.6 ± 0.2	0.58 ± 0.01	215 ± 1
RRAL-06_2	C	—	347 ± 2	(7)	−2.1 ± 0.1	(5)	3.5 ± 0.1	0.64 ± 0.01	151 ± 1

Table 3 (*continued*)

Sample	Inclusion appearance	Daughter mineral	Nb pts	Th (°C)	Nb pts	Tm$_{(ice)}$ or Tm$_{(hal)}$ (°C)	wt% NaCl eq.	Density (g/cm^3)[1]	Minimum pressure (bars)[2]
						San Blas vein, liquid-rich type			
RRAL-06_2	C	—	(3)	306 ± <1	(3)	−7.0 ± 0.1	10.5 ± 0.1	0.83 ± 0.01	89 ± 1
RSHA-04_2	C	—	(8)	309 ± 5	(8)	−1.9 ± 0.6	3.3 ± 1.0	0.72 ± 0.01	93 ± 7
RSHA-04_2	C	—	(7)	322 ± 5	(2)	−3.4 ± 0.1	5.5 ± 0.1	0.73 ± 0.01	111 ± 5
						San Blas vein, vapor-rich type			
RSHA-04	PS	—	(3)	369 ± 9	(3)	n.m.	n.m.	n.m.	n.m.
RSHA-04	PS	—	(2)	377 ± 9	(2)	−1.8 ± 0.2	3.1 ± 0.3	n.m.	n.m.
						San Blas vein, multiphase-solid type [3]			
RSHA-04	PS	Hl + op	(3)	310 ± 12	(3)	176 ± 14	30.8 ± 0.6	1.01 ± 0.02	76 ± 14
RSHA-04	PS	Hl + op	(2)	294 ± 5	(2)	232 ± 3	33.6 ± 0.2	1.06 ± 0.01	59 ± 4
RSHA-04	PS	Hl + op	(4)	394 ± 12	(4)	206 ± 27	32.3 ± 1.4	0.93 ± 0.02	200 ± 16
RSHA-04	PS	Hl + op	(2)	351 ± 26	(2)	263 ± 10	35.4 ± 0.6	1.01 ± 0.02	124 ± 37
RSHA-04	PS	Hl + op	(3)	325 ± 15	(2)	154 ± 1	29.8 ± 0.1	1.00 ± 0.01	86 ± 7
RSHA-04	PS	Hl + op	(3)	333 ± 2	(3)	274 ± 3	36.1 ± 0.2	1.04 ± 0.01	97 ± 2
RSHA-04	PS	Hl + op	(2)	323 ± 15	(2)	184 ± 27	31.2 ± 1.2	1.00 ± 0.01	92 ± 17
RSHA-04_2	C	Hl + op	(6)	328 ± 11	(4)	230 ± 30	33.5 ± 1.7	1.02 ± 0.02	96 ± 17
RSHA-04_2	C	Hl + op	(7)	307 ± 23	(7)	172 ± 11	30.6 ± 0.5	1.02 ± 0.02	76 ± 24
RSHA-04_2	C	Hl + op	(5)	326 ± 32	(5)	214 ± 16	32.6 ± 0.8	1.01 ± 0.05	99 ± 45
RSHA-04_2	I	Hl + op + tp	(2)	338 ± 28	(2)	235 ± 8	33.7 ± 0.5	1.01 ± 0.03	110 ± 36
RSHA-04_2	PS	Hl + op + tp	(3)	353 ± 24	(3)	294 ± 7	37.5 ± 0.5	1.04 ± 0.02	124 ± 32

Th = homogenization temperature, Tm$_{(ice)}$ = ice melting temperature, Tm$_{(hal)}$ = halite melting temperature, Nb pts = number of measurements, P = primary, PS = pseudosecondary, C = cluster, I = isolated, RD = randomly distributed in cloudy cores, Hl = halite, op = opaque phase, tp = transparent phase, — = not detected, n.m. = not measured.

[1] Calculated density of homogenized fluid in inclusions.

[2] Calculated minimum pressure value of entrapment.

[3] Tm$_{(hal)}$ for this type of inclusions instead of Tm$_{(ice)}$.

from the veins (Py$_v$). They show up to 50,000 ppm As, 1,000 ppm Co, Ni, and Cu; 100 ppm Mn, Zn, Ag, Sn, Sb, Te, Au, Pb, and Bi, and < 10 ppm V, Ga, Cd, In, and W (Table A3). Sedimentary pyrite (Py$_s$) is enriched in Co, Ni, Mo, V, Mn, Tl, Sb and Pb and depleted in Au and As, compared with hydrothermal pyrite from veins (Py$_v$) and hydrothermal pyrite disseminated in the host rock (Py$_h$) (Figs. 7, 8, A3, and A4). Pyrites from ore bodies (Py$_b$) are depleted in all trace elements, except Co and Ni, compared to sedimentary pyrite or hydrothermal pyrites in veins and disseminated in the sedimentary host rock (Figs. 8, A3, A4).

A statistical summary of gold concentrations in sulfides from the Algamarca deposit is illustrated in Fig. 8. All analyses on sedimentary pyrite (Py$_s$) are above the limit of detection (>0.03 ppm Au) with an average of 0.1 ppm Au. Gold concentrations in sulfides from ore bodies (pyrite, pyrrhotite and marcasite) are close to or below the limit of detection. In contrast, gold concentrations in hydrothermal pyrite from veins (Py$_v$) are well above the detection limit for most analytical points (96 %), with an average of 5 ppm Au and a maximum value of 160 ppm Au. Arsenopyrite shows an average of 4 ppm Au, with maximum of 320 ppm Au, which is the highest Au concentration among the analyzed sulfides. The 70 % of the Au analyses in chalcopyrite are below detection limit (<0.05 ppm), with a maximum value of 0.1 ppm. In tetrahedrite and tennantite, 30 % of the analyses are below detection limit (<0.05 ppm), most of the significant values are less than 0.2 ppm (with two exceptions of 0.5 ppm and 1.1 ppm in tetrahedrite). Pyrite disseminated in sedimentary host rocks (Py$_h$) has an average of 1.4 ppm Au with all datapoints above the detection limit; rims generally display higher Au concentrations than cores.

The analyses show that hydrothermal arsenian pyrite and arsenopyrite are the two sulfides with the highest invisible Au content (Fig. 8). Together with native gold, they are the major hosts of gold in the deposit. In arsenian pyrite, Au and As contents display a wedge-shape pattern below the empirical Au metal solubility limit (Reich et al., 2005) and a significant positive Au-As correlation at As contents in pyrite above 0.1 wt% (Fig. 7b). LA-ICPMS patterns from these pyrites generally show smooth and flat signals for Au suggesting the absence of nanoparticles of gold metal and/or other gold-bearing minerals (Fig. A5a, b). It is only in few cases that the Au signal presents a spiky pattern parallel to that of Te, corresponding to gold telluride inclusions (Fig. A5c, d). Bismuth signals in the LA-ICPMS patterns show matching sharp peaks with Te and positive correlations indicating that most of the Bi and Te in pyrite are contained in Bi-Te inclusions (Fig. A5a, b; Table A4). Elements such as Zn, Ga, Cd, In, and Sn show positive correlations between each other (Fig. A4g, h; Table A4). Similarly, positive correlations are shown by Co with Ni and Ag with Pb (Fig. A4a, f; Table A4).

The pyrite in veins from stage B (Py$_v$-II) shows higher As and invisible-gold contents than those in stage A (Py$_v$-I). Most of the gold contents in Py$_v$-II exceed 10 ppm Au, whereas they are consistently below 10 ppm in Py$_v$-I (Fig. 7b). Lead content exhibits the same trend as Au and As, with concentrations systematically higher in Py$_v$-II than in Py$_v$-I (Fig. A4f).

3.3. Fluid inclusion analyses

3.3.1. Fluid inclusion petrography and microthermometry

Four different types of fluid inclusions in quartz were identified in the Algamarca veins and ore bodies. Based on the major phases observed at room temperature, they were classified, according to the criteria of Shepherd et al. (1985), as i) immiscible-liquid (containing volatile phases, mostly carbonic, accompanied by H_2O), ii) multiphase-solid (H_2O plus solid phases), iii) vapor-rich (H_2O), and iv) liquid-rich (H_2O) (Figs. 9 and 10). Cathodoluminescence imaging reveals different quartz generations within the Algamarca veins. The Qz-I generation from stage A is brighter luminescing compared with the dark luminescing Qz-II generation from stage B (Fig. 11a, b). The results of microthermometry analyses are reported in Table 3, 4, and A5, and
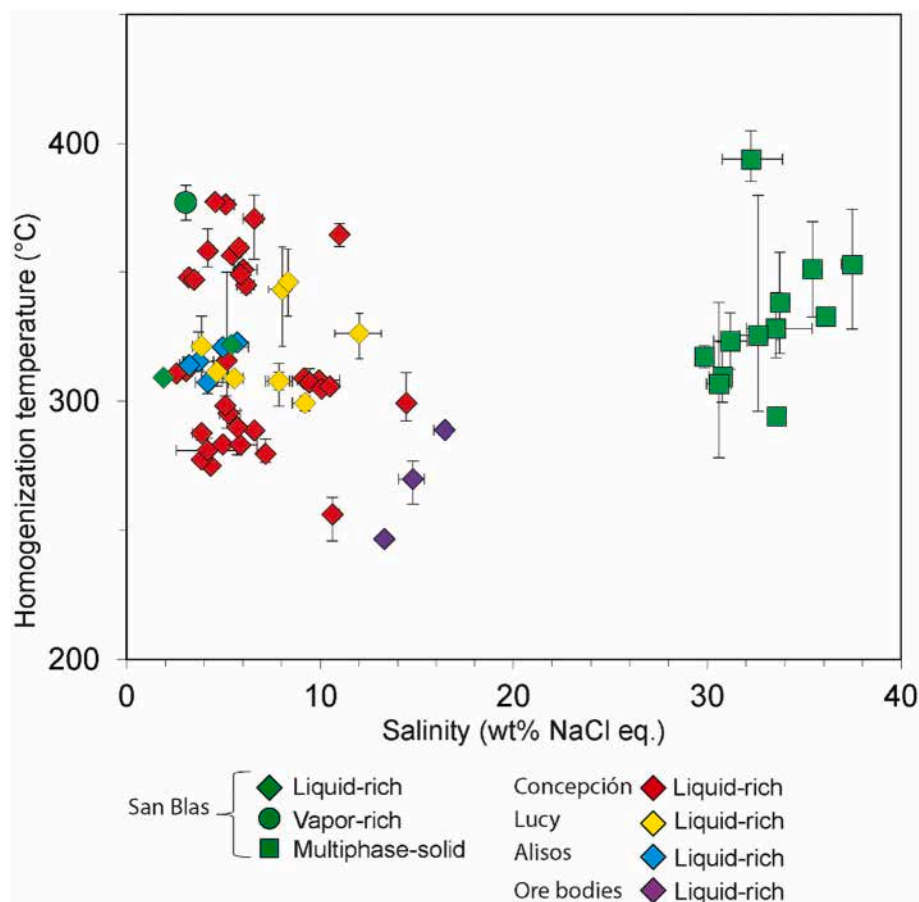
Fig. 12. Homogenization temperature (Th) vs. salinity for FIAs in quartz from stages A and B, from the Algamarca veins and ore bodies. Each point represents an average value of Th and salinity in a FIA; error bars correspond to the minimum and maximum value for each FIA (no error bars are shown where they are smaller than the symbol size).
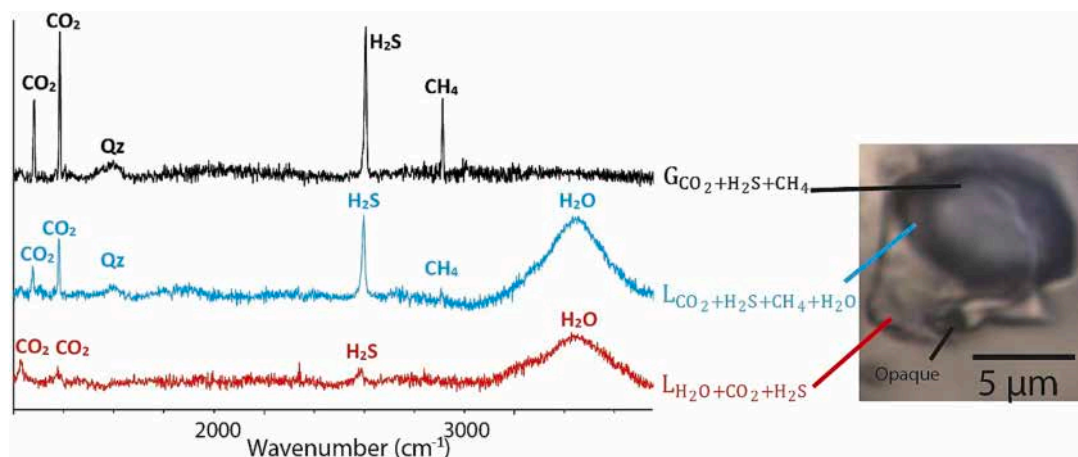

Fig. 13. Raman spectra of the different phases in a fluid inclusion representative of the immiscible-liquid type.

shown in Fig. 12 and A6. The composition of the different phases was determined by Raman spectroscopy (see section 4.3.2).

Pre-gold stage (Stage A). In Qz-I from Stage A of Algamarca veins three types of FIAs were recognized (i, ii, and iii; Fig. 10), which are described as follows. The immiscible-liquid type fluid inclusions (i) contain four phases at ambient conditions, including a CO_2-H_2S-CH_4 gas bubble, a CO_2-H_2S-CH_4-H_2O liquid, an aqueous liquid, and a small opaque daughter mineral (Fig. 9a). These fluid inclusions were found only in the San Blas vein, have an oval to irregular shape and a size of up

to 10 μm. They appear as clusters, pseudosecondary trails, or isolated individuals (e.g., Fig. 9a). The immiscible-liquid FIAs predate the multiphase-solid FIAs (see the following paragraph). Clusters of immiscible-liquid fluid inclusions are present in the core of quartz crystals (Qz-I) and are cross-cut by pseudosecondary and secondary trails of multiphase-solid fluid inclusions (not shown). Immiscible-liquid FIAs homogenize to vapor with homogenization temperature values (Th) from 404 to 498 °C (with one exception of 327 °C in an isolated fluid inclusion; Table A5), the opaque daughter mineral does not change

Table 4

Chemical composition acquired by Raman spectroscopy and corresponding microthermometric data for selected fluid inclusions of the immiscible-liquid fluid type in sample RSHA-04, from stage A (invisible-gold stage) in the San Blas vein.

Inclusion	Microthermometry				Raman data (mole % of volatile component)		
	$Tm_{(CO_2)}$ (°C)	$Th_{(CO_2)}$ (°C)	$Tm_{(clath)}$ (°C)	Th (°C)	CO_2	H_2S	CH_4
1	–67.1	30.9	10.2	460	63.2	26.8	10.0
2	–66.0	30.9	—	449	61.9	28.0	10.1
3	–66.3	31.0	12.5	484	60.3	31.7	8.0
4	–66.5	31.0	9.3	423	67.2	26.4	6.4

Th = homogenization temperature, $Tm_{(CO2)}$ = melting temperature of solid CO_2, $Tm_{(clath)}$ = melting temperature of clathrate, $Th_{(CO2)}$ = homogenization temperature of liquid CO_2, — = not measured.

during heating runs. The salinity, bulk composition and pressure values for this type of fluid inclusions could not be calculated from microthermometry or Raman data due to their high H_2S concentrations (revealed by Raman spectroscopy), which strongly affect the clathrate melting temperature (Touray and Guilhaumou, 1984), but are not accounted for in the model of Bakker (1997).

The second type of FIAs present in Qz-I, classified as multiphase-solid type (ii), contains multiple solid phases. They comprise a brine, a cubic crystal (halite), a vapor bubble, an opaque mineral, and a rounded greenish to transparent and slightly anisotropic mineral. The opaque mineral in these FIAs has a rounded shape or, less frequently, a pin-lke shape (Fig. 10). Multiphase-solid fluid inclusions have rounded or negative crystal shapes with sizes up to 20 μm. They occur as pseudo-secondary and secondary trails and clusters. The multiphase-solid fluid inclusions homogenize to liquid, and show previous halite dissolution. Other solids dissolve at lower temperatures than halite, except the opaque mineral that remains unchanged during heating. This type of FIAs has Th values from 294 to 353 °C (with a single outlier of 394 °C), and salinities from 30 to 38 wt% NaCl eq. (Table 3).

The third type of FIAs present in Qz-I consists of vapor-dominated fluid inclusions, referred to as vapor-rich (iii). These fluid inclusions were observed in Qz-I from San Blas vein and Lucy vein (cloudy cores; Fig. 9e, 10 and 11c). The vapor bubble occupies more than 60 % of the fluid inclusion volume, with remaining liquid and an opaque mineral sporadically observable in some inclusions. Vapor-rich fluid inclusions occur as clusters or, less frequently, associated with multiphase-solid fluid inclusions forming a boiling assemblage (Fig. 9e and 10). Because the liquid phase in vapor-rich fluid inclusions is scarce or visually absent, only few microthermometry measurements could be conducted (Table 3), yielding Th values of 369 and 377 °C (from 2 FIAs) and a salinity of 3 wt% NaCl eq. (from 1 FIA).

Gold-stage (Stage B). In Qz-II from Stage B of Algamarca veins, fluid inclusions are exclusively liquid-rich (type iv), with liquid occupying more than 60 % of the volume, accompanied by a vapor bubble (<40 %) and a tiny opaque daughter mineral (locally present in the Conception vein; Table 3). The liquid-rich fluid inclusions are present in quartz from Lucy, Concepción, Alisos, and San Blas veins and have oval, rounded or negative crystal shapes with sizes between ~2 and 20 μm (exceptionally reaching up to 50 μm in size). They occur as primary fluid inclusions parallel to growth bands and along pseudosecondary trails, as well as clusters, isolated individuals and along secondary trails (e.g., Fig. 9f and 11d-f). In addition, randomly distributed liquid-rich fluid inclusions were identified in cloudy cores of quartz in the Lucy vein (Fig. 11 c). These cores (Qz-I) are bright luminescing under cathodoluminescence imaging compared to the host quartz (Qz-II; Fig. 11b). The liquid-rich fluid inclusions in these cloudy cores correspond to an early generation that is "secondary" in origin with respect to the cloudy cores (Qz-I), and were formed before the liquid-rich fluid inclusions trapped in Qz-II. The latter are hereinafter referred to as late liquid-rich type.

All liquid-rich fluid inclusions homogenize to liquid. Liquid-rich FIAs from the Alisos, San Blas and Lucy veins homogenize at 300–320 °C and have salinities of 3–10 wt% NaCl eq. However, the early FIAs in the cloudy quartz core (Qz-I) of the Lucy vein present higher Th values and

salinities, 330–350 °C, and 8–14 wt% NaCl eq., respectively (Fig. A6). The Concepción vein has two populations of liquid-rich FIAs based on their Th. The first population presents Th values ranging from 260 to 310 °C and salinities from 3 to 14 wt% NaCl eq., not notably different from FIAs from the Alisos, San Blas and Lucy (late liquid-rich FIAs) veins. The second population presents higher Th values, of 350–380 °C and salinities of 3–11 wt% NaCl eq., comparable with the values in early liquid-rich FIAs from the cloudy cores in the Lucy vein (Fig. A6). The similarity in Th and salinity strongly suggests the presence of similar early liquid-rich FIAs in the Concepción vein (second population of FIAs), even though a clear temporal relationship between the two populations of FIAs in the Concepción vein could not be confirmed by petrographic features. Sedimentary clastic quartz grains, found in sandstones from the Chimú Formation, are distinguishable by their round shapes and high luminescence, present small liquid-rich fluid inclusions (<5 μm) with Th values around 285 °C, as measured in a single quartz grain.

In the San Blas vein that contains all four fluid inclusion types, the earlier immiscible-liquid fluid inclusion type (present in Qz-I) shows the highest Th values, up to 500 °C; however, pressure correction could not be applied. In this quartz type, the multiphase-solid fluid inclusions show Th values of 300–400 °C and coexist with vapor-rich fluid inclusions, which suggests boiling. Hence, no pressure correction is required for obtaining the actual entrapment temperature of these types of fluid inclusions. Finally, liquid-rich fluid inclusions found in Qz-II (Stage B) record Th values of ~315 °C. At this stage, shallow deposition is expected, which is characteristic for epithermal mineralization. Therefore, the pressure correction for these data is likely to be minimal, in agreement with the temperature of ~325 °C estimated in the invisible-gold substage using arsenopyrite geothermometry (Kretschmar and Scott, 1976).

Pyrrhotite-stage (Stage A). In quartz from Algamarca ore bodies only liquid-rich FIAs were identified. Opaque minerals were not observed; the vapor bubble occupies <20 % of the inclusion volume. They appear as secondary and pseudosecondary trails, clusters, or isolated fluid inclusions, mostly <10 μm in size. They present lower Th values than liquid-rich FIAs in quartz from Algamarca veins, from 250 to 290 °C, and higher salinities, from 13 to 16 wt% NaCl eq. (Fig. 12).

3.3.2. Raman spectroscopy of fluid inclusions

In immiscible-liquid fluid inclusions, the melting temperature point of solid CO_2 ranges from –67.7 to –65.0 °C, and the clathrate melting point reaches 12.1 °C (Tables 4 and A5), indicating that other significant components accompany the dominant CO_2 (Bodnar et al., 2014). Therefore, Raman analyses were performed on those fluid inclusions to detect such components. Carbon dioxide (CO_2) was clearly detected by its Fermi dyad bands at 1282 and 1385 cm^{-1} in the vapor phase, at 1276 and 1381 cm^{-1} in the liquid carbonic phase, and at 1279 and 1381 cm^{-1} in the aqueous liquid phase (Fig. 13; e.g., Burke, 2001; Frezzotti et al., 2012). In addition, H_2S and CH_4 were detected, respectively, by their S-H and C-H symmetric stretch vibrations respectively at 2604 and 2913 cm^{-1} in the vapor CO_2-dominated phase, and at 2597 and 2907 cm^{-1} in the liquid CO_2 phase (Fig. 13; Dubessy et al., 2012). In the aqueous
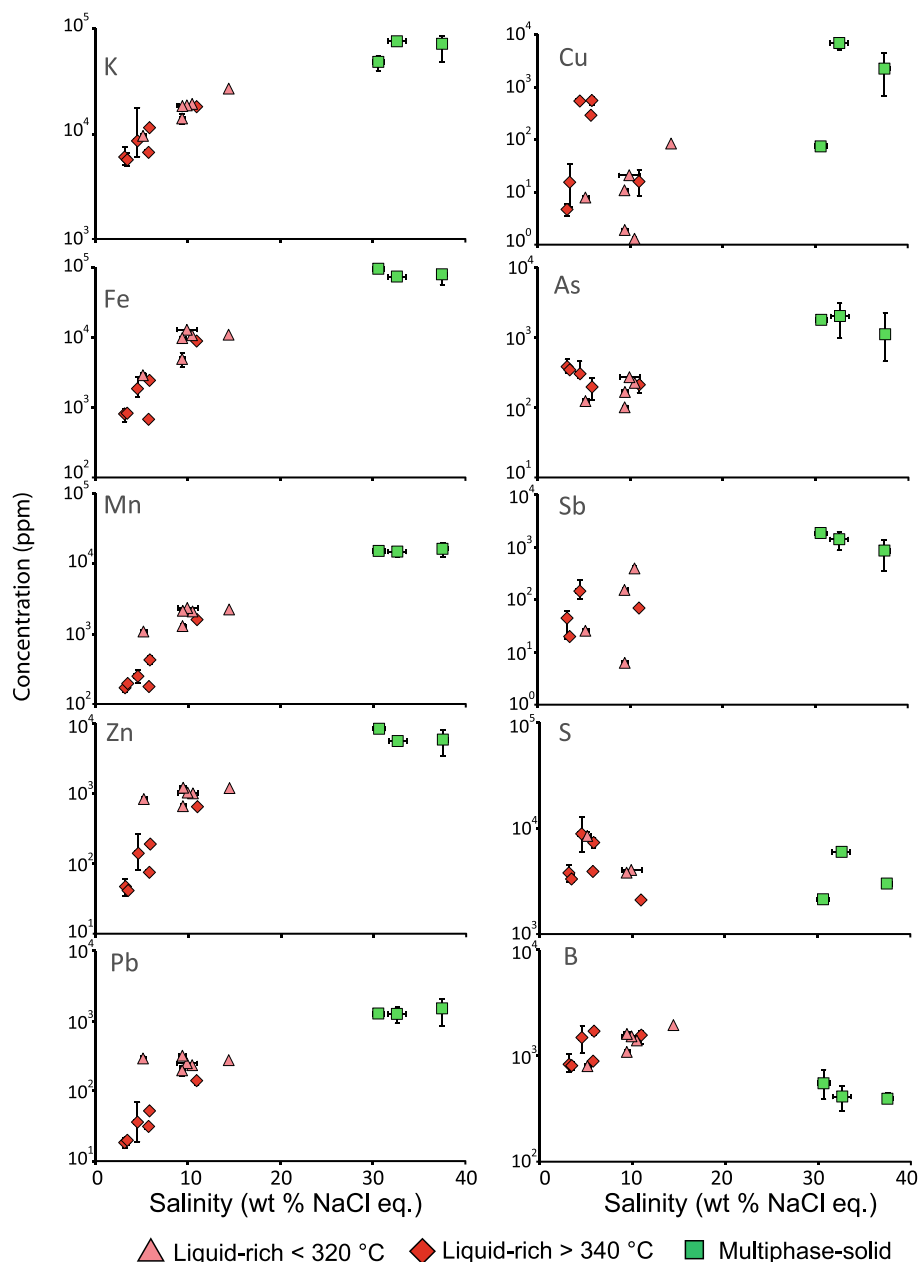
Fig. 14. Selected element concentrations vs. salinity for FIAs from the Concepción and San Blas veins. Each point represents an average value in a FIA; error bars correspond to the minimum and maximum value for each FIA (no error bars are shown where they are smaller than the symbol size or only one measurement is available).

liquid phase, H$_2$S was detected at 2585 cm^{-1} (Fig. 13). The identified H$_2$S peak wavenumbers are in excellent agreement with those known in the gas, liquid and aqueous phases (Pokrovski and Dubessy, 2015; references therein). Raman analyses of peak ratios in the gas phase (Burke, 2001) show the mole percentage of CO$_2$ in the carbonic vapor phase ranging from 60.4 to 67.2 %, H$_2$S from 26.4 to 31.7 %, and CH$_4$ from 6.4 to 10.1 % (Table 4).

No other sulfur species such as sulfate or polysulfides were detected in the aqueous liquid phase of our fluid inclusions. Sulfate may be either minor in the fluid due to relatively reduced conditions and/or taken by some of the solid phases observed in the fluid inclusions. No attempt was made in this study to specifically acquire Raman spectra on heating of fluid inclusions that might potentially reveal other sulfur species existing in aqueous solution at higher temperatures such as the trisulfur radical ion (Jacquemet et al., 2014; Pokrovski and Dubessy, 2015; Barré et al., 2017).

Raman analyses in the vapor phase of two vapor-rich and one multiphase-solid fluid inclusions did not detect CO$_2$ or the other gases. Raman spectra of the small opaque mineral (with spherical shape) in one multiphase-solid fluid inclusion indicate that it is likely to be chalcopyrite.

3.3.3. LA-ICPMS analyses of fluid inclusions

Twenty-six individual liquid-rich fluid inclusions from 12 fluid inclusion assemblages (each one including 1 to 6 individual fluid inclusions) were analyzed in quartz from stage B (Qz-II) from the Concepción vein. The concentrations of B, Na, K, Mn, Fe, Zn, Sr, Cs, and Pb exceed the detection limit in all fluid inclusions. Other elements, such as Mg, Ca, As, Cu, Sb, Cl, and S, exceed their detection limits in >70 % of the fluid inclusion analyses. Silver was detected in 50 % of the fluid inclusions and Au was only detected in one fluid inclusion. The average element concentrations of each fluid inclusion assemblage are reported
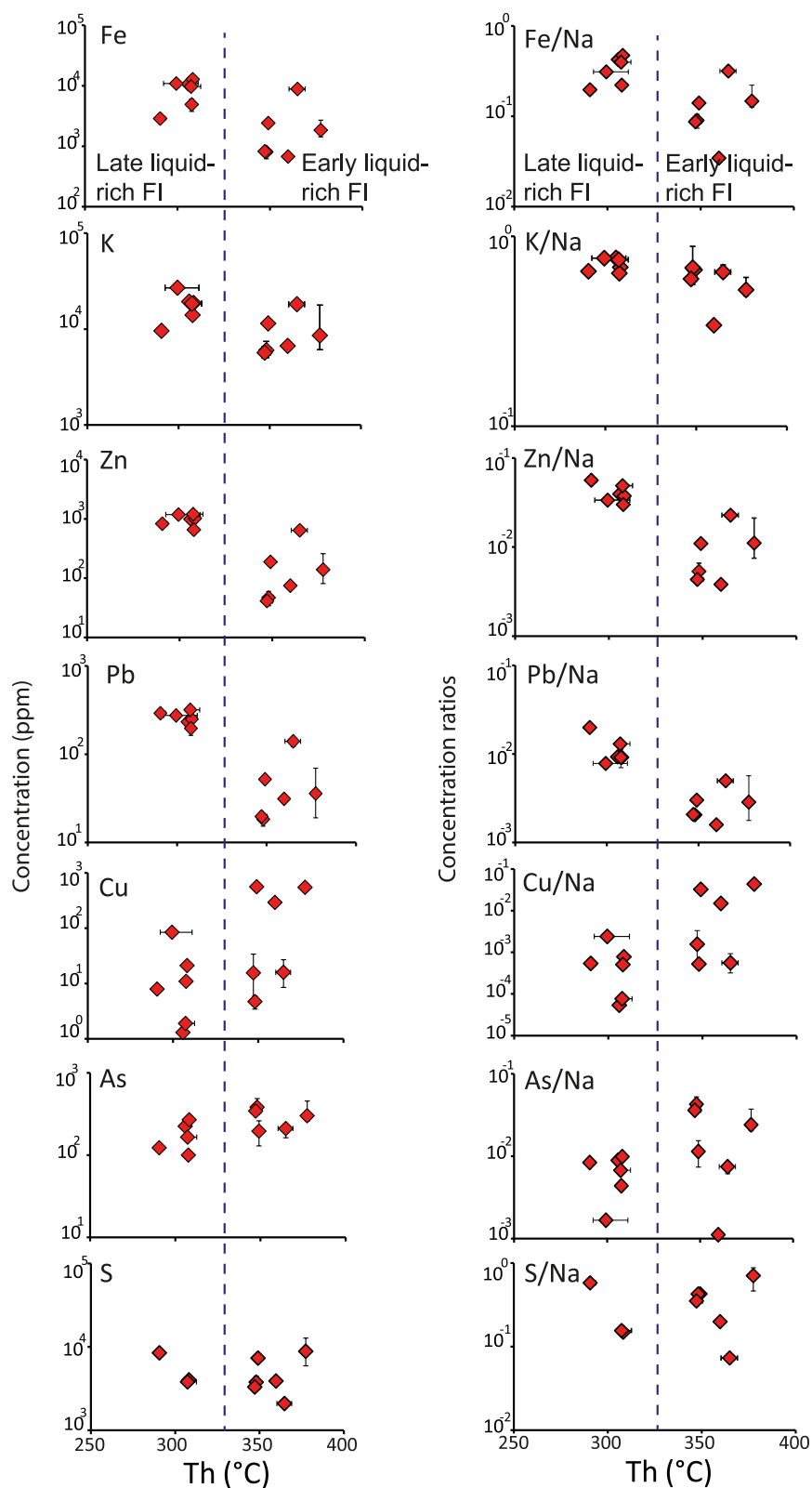
Fig. 15. Selected element concentrations and element concentration ratios (X/Na) for liquid-rich FIAs vs. Th from the Concepción vein (see Fig. 14 caption for more details).
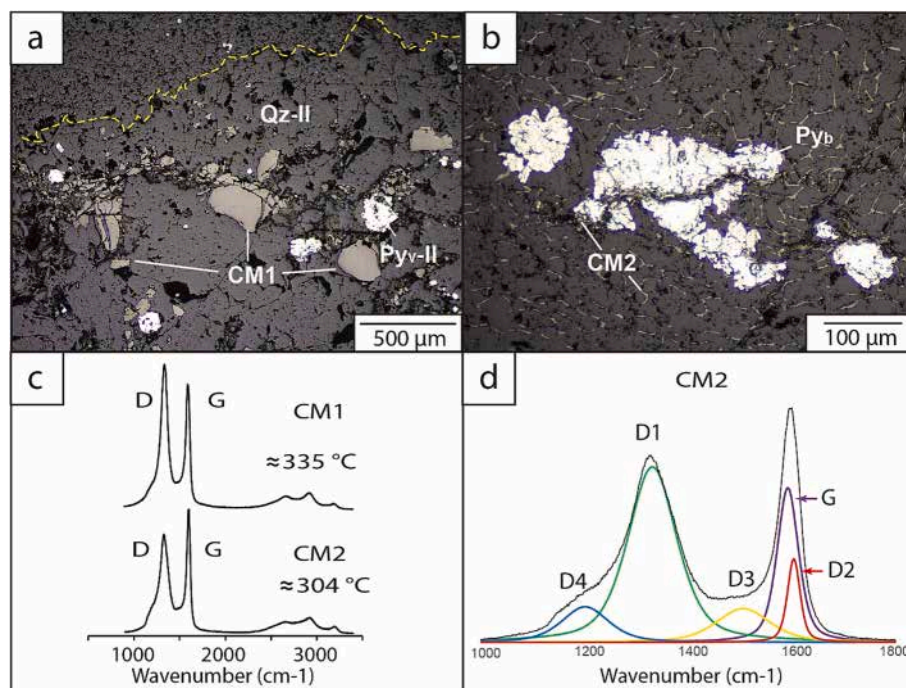
Fig. 16. Photomicrographs and Raman spectra of carbonaceous material (CM1 and CM2) from the Algamarca deposit. (a) Quartz vein hosting CM1 and pyrite. The yellow dotted line marks the contact between the sedimentary host rock and the vein. (b) Thin irregular bands of CM forming kind of a mesh, together with anhedral pyrite. (c) Raman spectra of CM1 and CM2. (d) An example of peak fitting of a Raman spectrum.
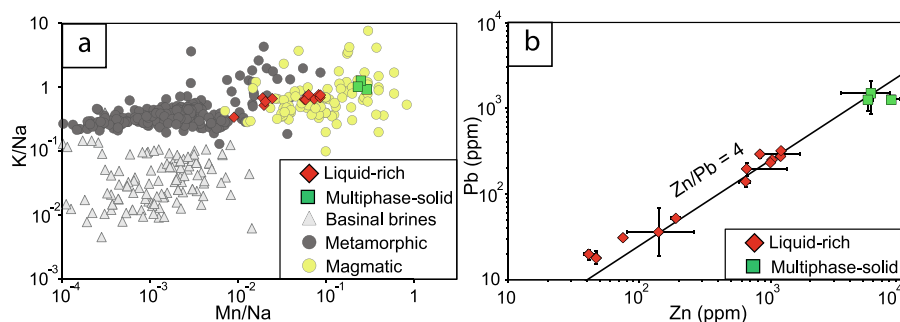

Fig. 17. LA-ICPMS data obtained from liquid-rich and multiphase-solid FIAs (red and green, respectively) and comparison with literature data. (a) K/Na vs Mn/Na ratios in FIAs from Algamarca veins, as well as from typical basinal brines (Samson et al., 2008; Zou et al., 2020; Sośnicka et al., 2023), metamorphic (Rauchenstein-Martinek et al., 2016) and magmatic fluids (Williams-Jones et al., 2010; Kouzmanov and Pokrovski, 2012). (b) Pb vs Zn element concentration in FIAs from Algamarca veins. The linear fit to the datapoints corresponds to a Zn/Pb ratio of 4. Error bars correspond to the minimum and maximum value within each FIA.

in Table A6 and plotted in Figs. 14 and 15. The most abundant elements in liquid-rich fluid inclusion assemblages (in the order of decreasing mean concentration) are Cl, Na, K, Fe, Ca, and S reaching up to 10,000 ppm levels, followed by moderately-abundant B, Mn, Mg, and Zn (up to 2,000 ppm), and by less abundant Cu, As, Sb, Pb, Cs, and Sr (between 100 s and 10 s ppm), and, finally, Ag (<5 ppm), and Au ($\leq$0.2 ppm). Positive correlations were observed between the salinity and the concentration of analyzed elements in liquid-rich fluid inclusions except for S, B, Cu, As, and Sb (Fig. 14). Late liquid-rich FIAs show higher Fe, K, Zn, and Pb concentrations and their corresponding element/Na ratios than early liquid-rich FIAs; in contrast, Cu and As concentrations and their corresponding element/Na ratios are lower (Fig. 15). Individual early liquid-rich fluid inclusions reach 650 ppm Cu and 490 ppm As, while late liquid-rich fluid inclusions show <80 ppm Cu and <270 ppm As. The concentration of S (0.1–1 wt%) is similar in both generations of liquid-rich fluid inclusions (Fig. 15).

In quartz of stage A (Qz-I) from the San Blas vein, eight multiphase-solid fluid inclusions from three FIAs were analyzed. The other types of fluid inclusions present in Qz-I (immiscible-liquid and vapor-rich,

examined by microthermometry) were not analyzed by LA-ICPMS because no suitable fluid inclusions were found, their scarcity and small size being the main impediments for quantitative measurement of trace element contents. In all multiphase-solid fluid inclusions, the concentrations of B, Na, Mg, Cl, K, Ca, Mn, Fe, Zn, As, Rb, Sr, Ag, Sb, Cs, Ba, Pb, and Bi exceed the detection limit. Other elements such as Cu, Br, S, and Mo exceed the detection limit in more than half of the analyses. Gold was not detected in any fluid inclusion. The most abundant elements in multiphase-solid FIAs are Cl, Fe, Na, K, and Mn, always showing concentrations of >1 wt%, followed by Zn (up to 0.8 wt%), Cu and Ca (up to 0.7 wt%), and S (up to 0.6 wt%). Minor, but omnipresent, elements are Sb, As, and Pb (reaching 1,000 ppm levels), followed by Rb, Br, B, Bi, Sr, Cs, Ba, Ag (100 s ppm), and Mo < 1 ppm. No trends for these elements could be identified likely due to the too small number of FIAs analyzed and to too narrow a range in salinity and homogenization temperature. The concentrations of elements in multiphase-solid fluid inclusions are higher than in liquid-rich fluid inclusions, except for S and Mg showing similar contents and for B being slightly lower (Fig. 14; Table A6).
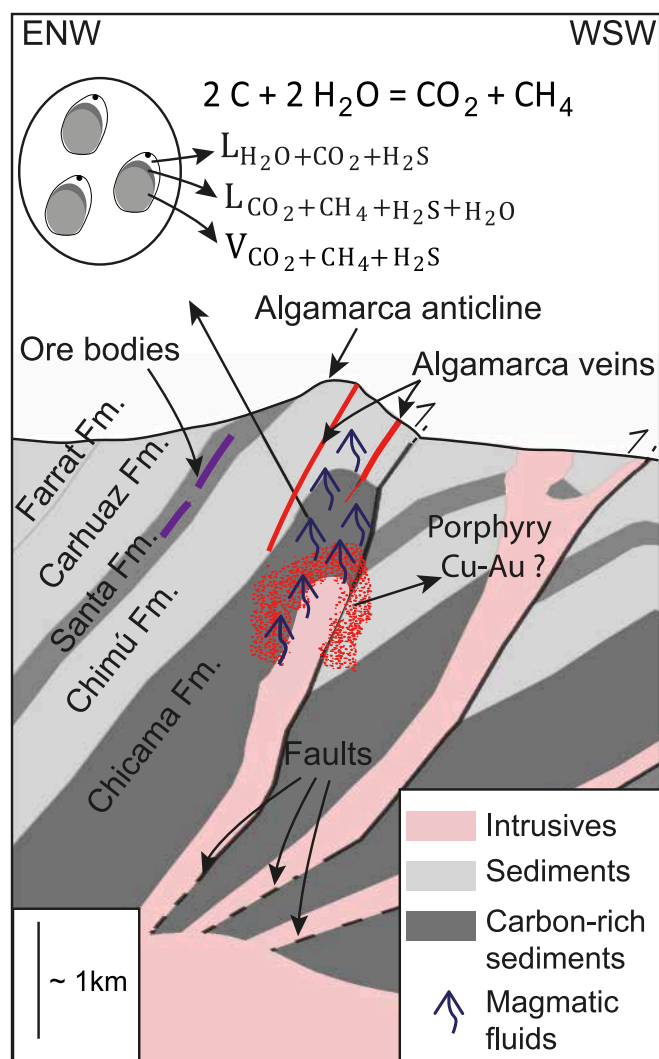
Fig. 18. Conceptual model of the Algamarca deposit formation. Immiscible-liquid fluid inclusions result from the interaction between magmatic fluids and the carbon-bearing sediments from the Chicama Formation (Fm.). These interactions, coupled with favorable tectonics (faults, anticlines), greatly favored gold transport through the sedimentary sequence and subsequent gold accumulation in arsenian pyrite.

3.4. Raman spectra of carbonaceous material (CM)

The Raman spectra of CM were collected on three representative polished sections, one from sample RRAL-07 (CM1) and two from sample RRAL-14 (CM2). The CM in sample RRAL-07 is present in narrow quartz-pyrite veins (<1 cm) with subordinate tennantite-tetrahedrite and chalcopyrite, all minerals from stage B of the Concepción vein hosted by shales of the Chimú Formation (Fig. 16a). The CM in sample RRAL-14, collected in a fault zone of the Santa Formation next to the Algamarca ore bodies, is present in quartz and pyrite assemblages as disseminations and irregular interconnected bands (Fig. 16b). Potential effects on the Raman spectra of CM that might be induced by the polishing or different orientation were assumed to be negligible because the CM analyzed in this work presents a relatively low degree of graphitization at which such effects are small to negligible (Kouketsu et al., 2014, Hu et al., 2015; references therein). It can be seen in Fig. 16c that the relative intensities of the G-band versus the D-band are distinctly different in CM1 and CM2 samples, with the G-band being more intense in CM1, implying higher degree of graphitization of CM1 compared to CM2 (Lahfid et al., 2010). The graphitization peak temperature may be

quantified from these Raman peak parameters (Beyssac et al., 2002). Several geothermometers have been proposed for high and low-grade metamorphism (e.g., Beyssac et al., 2002; Rahl et al., 2005; Lahfid et al., 2010; Kouketsu et al., 2014). More recently, their application has been extended to sedimentary-hosted gold deposits (e.g., Hu et al., 2015; Wu et al., 2018). We used the geothermometers proposed by Lahfid et al. (2010) and Kouketsu et al. (2014). Fig. 16d shows an example of decomposition of a Raman spectrum of CM2 in five bands (G, D1, D2, D3, and D4); the obtained parameters and resulting temperature values are reported in Table A7.

In the Concepción vein of stage B, the homogenization temperatures measured in late liquid-rich fluid inclusions (360 ± 20 °C) are similar within errors to the temperature obtained from the carbonaceous material CM1 (335 ± 40 °C). The CM-measured values directly reflect the temperature of the fluid that interacted with the carbonaceous material, and was trapped in the inclusions in quartz. The similarity of these independent temperature estimations further supports the validity of our entrapment temperature values for which pressure correction is negligible, implying that the fluid was entrapped at relatively shallow levels (<1.5 km). This conclusion is in accordance with shallow environments typical of epithermal deposits (White and Hedenquist, 1995; Hedenquist et al., 2000; Simmons et al., 2005), and is also reflected in the textures of open space deposition displayed in the veins in stages B and C (Fig. A1a-d). Same as in the Concepción vein, in the ore bodies, the homogenization temperature in liquid-rich fluid inclusions (270 ± 20 °C) and Raman-measured temperatures in CM2 (305 ± 40 °C) overlap within errors, confirming shallow depths (<1.5 km) of formation.

4. Discussion

4.1. Properties, origin, and evolution of the mineralizing fluids

Algamarca and the other deposits located within the MFTB are associated with subduction-related Oligo-Miocene magmatic arc intrusions (Noble and McKee, 1999; Bissig and Tosdal, 2009). Thus, the different types of ore deposits in this belt likely reflect the large range of conditions intrinsic to porphyry systems associated with a magmatic activity (e.g., Sillitoe, 2010). Consequently, a magmatic source is commonly assumed for the mineralizing fluids (e.g., Rainbow et al., 2005; Cerpa et al., 2013; Rottier et al., 2018; Vallance et al., 2024). Our study directly supports a magmatic fluid origin for the Algamarca deposit based on fluid inclusion data, allowing to distinguish it from other potential sources such as metamorphic or basinal fluids, all of which are characterized by distinct elemental signatures (e.g., Samson et al., 2008; Nahnybida et al., 2009; Large et al., 2016).

The following lines highlight the evidence pointing to a magmatic origin of the Algamarca fluids. Firstly, the multiphase-solid fluid inclusions from Algamarca display high salt (NaCl, KCl) and metal (Fe, Cu, Zn) contents, which are diagnostic of magmatic brines from porphyry deposits (e.g., Kouzmanov and Pokrovski, 2012; Schirra et al., 2022). Secondly, the molar Br/Cl ratio obtained from the previously mentioned fluid inclusion type is $0.9 \ (\pm0.1) \times 10^{-3}$, which is distinctly lower than that of seawater (1.5×10^{-3}), and consistent with the typical range of magmatic fluids (0.5 to 1.0×10^{-3}; e.g., Kendrick et al., 2001; Nahnybida et al., 2009; references therein). Thirdly, the elevated Rb concentrations (500–1,000 ppm) in this fluid inclusion type are characteristic of magmatic fluids. Such fluids are enriched in Rb (>1,000 ppm Rb; Samson et al., 2008; Williams-Jones et al., 2010; Large et al., 2016; Zhao et al., 2020), and are systematically higher than values reported for basinal brines (<100 ppm; Samson et al., 2008; references therein) or metamorphic fluids (<140 ppm; Van Daele et al., 2018; references therein). Fourthly, the K/Na and Mn/Na ratios for multiphase-solid and liquid-rich fluid inclusions from Algamarca are higher than for basinal brines and metamorphic fluids (Fig. 17a; Samson et al., 2008; Williams-Jones et al., 2010). Finally, the liquid-rich and multiphase-solid fluid-inclusion types show overlapping Zn/Pb ratios of 5 ± 1 and 3 ± 1,

respectively (Fig. 17b), close to those reported for large porphyry deposits (Kouzmanov and Pokrovski, 2012; Rottier et al., 2016b). Furthermore, it is unlikely that the ratios of those pretty soluble elements that mostly stay in the fluid would have been significantly altered due to mechanisms such as boiling, sulfide precipitation and/or water-–rock interactions. As a result, their geochemical signatures clearly indicate a magmatic origin.

An uncommon feature of our fluid inclusion data set is the presence of immiscible-liquid fluid inclusions, displaying high CO_2, CH_4 and H_2S concentrations (mole percentage in the vapor phase of 60 %, 10 % and 30 %, respectively). Such high carbon volatile concentrations are quite unusual in a porphyry system. Although CO_2 was identified in several both oxidized and reduced porphyry systems (Shen et al., 2010), its concentrations estimated in fluid inclusions from typical porphyry systems are rather low (<10 mol%; Rusk et al., 2008; Catchpole et al., 2015). The scarcity of CO_2 is due to the low CO_2 solubility in magmas at shallow depths (Lowenstern, 2001), with the exsolution of most CO_2 from magmas occurring deeper in the crust in the early stages of a calc-alkaline magma evolution, in contrast to water and associated dissolved metals and salts that degas at shallower levels (Audétat and Simon, 2012). However, dissolution of carbonate-bearing sediments might also account for the presence of CO_2 in some hydrothermal fluids (e.g., Minissale et al., 2002), but requires the presence of carbonate rocks which are rare at Algamarca. Methane-bearing fluid inclusions are not reported in oxidized porphyry deposits (Rusk et al., 2008; Shen et al., 2010), while methane-rich inclusions are frequent in reduced porphyry deposits (Cao et al., 2014b; Zhang et al., 2019). In most cases, the origin of methane has been attributed to thermal decomposition of sedimentary organic matter. This decomposition can be generated by i) the deep burial of sediments in a typical petroleum system (Magoon and Dow, 1994), ii) contact metamorphism (e.g., Aarnes et al., 2010), or iii) magmatic assimilation (e.g., Iacono-Marziano et al., 2012; Capriolo et al., 2021). Other origins have also been invoked, including production of methane by a Fischer-Tropsch synthesis in which CO_2 is reduced to CH_4 (e.g., Cao et al., 2014a), microbial reactions (e.g., Ueno et al.,2006), or CH_4 being directly derived from the mantle (Cao et al., 2014a; references therein). Alternatively, methane as well as CO_2 may be generated by direct sedimentary organic matter interactions with hydrothermal fluids (e.g., Vallance et al., 2003; Fan et al., 2004; Zhu et al., 2012; Lang et al., 2020; Vallance et al., 2024). The latter mechanism seems to be most plausible in the context of Algamarca as discussed below.

Indeed, in the case of Algamarca—an epithermal deposit associated with an oxidized calc-alkaline magmatism—the composition of the immiscible-liquid fluid inclusions is highly unusual, with large and comparable amounts of coexisting CO_2, CH_4 and H_2S. A plausible explanation for this composition is that ascending magmatic fluids directly interacted with the carbon-bearing sediments, most likely from the Chicama Formation (Fig. 18). This would have led the production of both CO_2 and CH_4, by carbon disproportionation reaction in water such as

$$2 \text{ Graphite} + 2 \text{ H}_2\text{O} = \text{CO}_2 + \text{CH}_4 \tag{1}$$

Additional dissolution of hydrocarbons, richer in H (CH_x), would result in CH_4/CO_2 ratios higher than 1 in the fluid. Mixing of the hydrothermal fluids with CH_4 produced by thermogenesis of organic matter before or during the magmatic activity could also supply some CH_4. Hydrogen sulfide may stem from original S-rich magmatic fluids and/or petroleum-related H_2S, both known to be able to carry up to several wt % of sulfur (Kouzmanov and Pokrovski, 2012; Migdisov et al., 2017). The systematically lower CH_4/CO_2 (and /CH_4/H_2S) ratios recorded in the immiscible-liquid fluid inclusions (Fig. 13) compared to those produced by reaction (1) and the other mechanisms discussed above, are fundamentally due to much lower CH_4 than CO_2 or H_2S gas solubility in aqueous solution. Indeed, $CH_{4(g)}$ is at least 10 and 30 times

less soluble in liquid water than $CO_{2(g)}$ and $H_2S_{(g)}$, respectively, according to the well-known thermodynamic Henry constants of the reactions $CH_{4(g)} = CH_{4(aq)}$, $CO_{2(g)} = CO_{2(aq)}$, and $H_2S_{(g)} = H_2S_{(aq)}$ (e.g., Naumov et al., 1971; Akinfiev and Diamond, 2003). As a result, methane produced by reaction (1) or similar would have a stronger tendency than CO_2 (and H_2S) to exsolve from the fluid into the gas phase and to leave the system before quartz growth and fluid inclusion entrapment, resulting in CH_4/CO_2 ratios less than 1, as we systematically found in fluid inclusions (Table 4). The strong interactions between the carbon-bearing sediments and the hydrothermal fluid are also reflected in the structure of the carbonaceous material, which yields a temperature value for peak metamorphism similar to those recorded for the fluid inclusions.

Interactions of magmatic fluid and carbonaceous material are likely to be common in subduction-related magmatic arc settings such as for the Miocene metallogenic belt of central and northern Peru. For example, the occurrence of low-sulfidation assemblages in epithermal deposits, like Cerro de Pasco and Shahuindo, was interpreted by interactions of the magmatic fluid with the carbonaceous material from the basement or from the sedimentary host rock (Rottier et al., 2016a, 2018; Vallance et al., 2024). Indeed, the immiscible-liquid fluid inclusions from the Algamarca deposit offer irrefutable proof of these intensive interactions. Beyond the above examples, the occurrence in the MFTB of Miocene low-sulfidation epithermal deposits, such as the Tres Cruces deposit (Montgomery, 2012) also likely reflects interactions of oxidized porphyry fluids, typical of calc-alkaline magmatism (Sillitoe and Hedenquist, 2005; Sillitoe, 2010), with the carbonaceous material of the Mesozoic sediments.

4.2. Trace elements in pyrite

The different types of pyrites found in the Algamarca deposit, i.e. in sedimentary rocks, ore bodies veins and host rocks (Py_s, Py_b, Py_v and Py_h), show differences in their textures and element concentrations (Fig. 5a-i, 7a, b, A3; Table 2). The sedimentary pyrite type is enriched in trace elements such as Co, Ni, Mo, V, Mn, Sb, and Pb (Fig. A3), which is consistent with the trace element patterns reported for sedimentary pyrite in black shales worldwide (e.g., Gregory et al., 2015). On the other hand, hydrothermal pyrite found in veins as well as disseminated in the host rock (Py_v and Py_h) is enriched in Au and As. Both elements show statistically positive correlations (Table A4), their concentrations in pyrite plot below the empirical gold solubility limit (Fig. 7b) proposed by Reich et al. (2005), and their LA-ICPMS transient signals are flat for most analyses (e.g., Fig. A5a, b). These features collectively indicate that Au is structurally bound in pyrite. The pyrite type from ore bodies was formed by replacement of pyrrhotite and marcasite, and shows the lowest Au and As concentrations, indicating that the replacement process appears to be less efficient in the incorporation of Au and As in pyrite than direct crystallization from the hydrothermal fluid.

In our paragenetic sequence, we have defined two main mineralization events, i.e., stages A (pre-gold stage) and B (gold stage), in which were found the pyrite types Py_v-I and Py_v-II, respectively. The concentration of Au and As in pyrite from stage B (Py_v-II; epithermal stage) is higher than in pyrite from stage A (Py_v-I; porphyry-like stage; Fig. 7a, b), which is also the case for many porphyry systems (e.g., Deditius et al., 2014; Franchini et al., 2015; Sykora et al., 2018). This feature thus supports a porphyry-epithermal transition for Algamarca.

4.3. Metal concentrations in the mineralizing fluid

During unmixing of a magmatic fluid to brine and vapor, Cu is partitioned preferentially into the brine, as it is shown by direct experimental measurements of vapor/liquid partition coefficients (Lerchbaumer and Audétat, 2012; Pokrovski et al., 2013; Kokh et al., 2016; Zajacz et al., 2017) and by the high Cu concentrations measured in brine inclusions from several porphyry deposits (0.5 wt% Cu in average;

Kouzmanov and Pokrovski, 2012; Schirra et al., 2022). Additionally, Cu concentrations in the brine-like and, more importantly, in vapor-like fluid inclusions might be modified, after fluid inclusion entrapment, by selective Cu diffusion through quartz lattice (Lerchbaumer and Audétat, 2012). Chalcopyrite precipitation processes from the brine phase may also contribute to variability of Cu concentrations in the fluid inclusions (e.g., Catchpole et al., 2011). At stage A of the Algamarca vein formation, quartz, pyrite, and chalcopyrite co-precipitated, and the most abundant fluid inclusions are multiphase-solid and vapor-rich types. At some places, the two types are present in the same assemblage, indicating that boiling occurred. The different FIAs show Cu concentrations varying from one FIA to another (from 70 to 7,000 ppm; Table A6), but similar Cu concentrations within a given FIAs, ruling out heterogeneous chalcopyrite entrapment during inclusion formation. Rather, the variability of Cu concentrations among the different FIAs may be due to a combination of chalcopyrite precipitation from the fluid during quartz growth and before fluid inclusion entrapment generated by cooling and fluid unmixing processes (e.g., Hezarkhani et al., 1999; Harris et al., 2005), coupled with possible post-entrapment Cu diffusion in or out the inclusion (Lerchbaumer and Audétat, 2012).

At stage B, the metal concentrations (Fe, K, Mn, Zn, Pb) of the liquid-rich fluid inclusions positively correlate with the salinity values (Fig. 14), as it would be expected for metals transported by chloride complexes (Kouzmanov and Pokrovski, 2012). The exception is Cu that does not show such correlations, which is likely related to the large Cu concentration variability in fluid inclusions as discussed above. Metalloids, such as As and Sb, do not show correlations with salinity values (Fig. 14), which is due to the fact that these elements are transported as hydroxide complexes (Pokrovski et al., 1996; Zotov et al., 2003). Despite the fall in temperature recorded by early to late liquid-rich FIAs (Fig. A6a), Zn and Pb are almost constant in the fluid (Fig. 15), indicating that saturation was not reached for these metals and in agreement with the absence of sphalerite and galena in the mineral assemblages (Fig. 4a), due to the relatively high solubility of ZnS and PbS over a wide range of temperature (Fontboté et al., 2017; references therein).

4.4. Role of arsenian pyrite in the gold concentration and deposition

The close association of Au and As in pyrite has been widely documented in several types of ore deposits (Deditius et al., 2014; references therein). It has recently been demonstrated that the coupled incorporation of Au^{II} and As^{-I} in the Fe and S pyrite crystallographic sites, respectively, is the key mechanism to explain the Au-As chemical association in arsenopyrite and arsenic-rich pyrite (Pokrovski et al., 2021). The extremely efficient partitioning into pyrite of Au and As from a fluid under-saturated with respect to metallic gold leads to large concentrations of Au and As chemically bound in pyrite at redox and pH conditions of Carlin and orogenic-type deposits (Kusebauch et al., 2018, 2019; Pokrovski et al., 2021), conditions that are similar to those determined at Algamarca.

The pyrite-fluid partition coefficients of Au and As are ~200 for both elements, as follows from the typical ratio of their concentrations in pyrite (Py$_v$-II) and in the liquid-rich type of fluid inclusions trapped in quartz (Qz-II) because both pyrite and quartz crystallized contemporaneously in the Algamarca veins. These partition coefficient values are of the same order of magnitude as those experimentally measured by Kusebauch et al. (2019) at 200 °C under redox and acidity conditions of Carlin-type deposits, and those predicted at higher temperatures, between 300 and 450 °C, by Pokrovski et al. (2021) under redox conditions for reduced porphyry and orogenic-type deposits. The enhanced Au partitioning into arsenian pyrite at our conditions allows for efficient gold scavenging even from fluids that are poor in Au (<0.1 ppm) as analyzed by LA-ICPMS in this study.

In the invisible-gold substage (B1), scavenging of Au from unsaturated fluid by arsenian pyrite is liable to be the main mechanism controlling Au deposition. In contrast, in the visible-gold substage (B2),

most gold was likely deposited as native metal. This difference may partly be related to more oxidizing conditions of sub-stage B2, manifested by the transition from low- (sub-stage B1) to intermediate-sulfidation state assemblage (sub-stage B2; Fig. 4a), conditions less favorable for both Au and As incorporation in pyrite in a chemically bound state (Pokrovski et al., 2021). Gangue minerals coeval to the native gold deposition were not found, which does not allow us to unambiguously constrain the causes for visible gold deposition. Generally, in most epithermal gold deposits, the major causes responsible for metallic gold deposition is the fluid boiling and the removal of H_2S into the vapor (Pokrovski et al., 2014; Simmons et al., 2020). Uplift and erosion are two processes that took place simultaneously during the formation of the Algamarca deposit. These events may have resulted in a pressure drop, thereby triggering fluid-phase separation during the visible-gold substage mineralization event (B2). This mechanism mainly removes H_2S from the liquid phase, destabilizing gold hydrosulfide complexes and allowing the precipitation of gold in a native state.

4.5. Role of the carbonaceous material in the gold transport and deposition

In an epithermal setting, genetically associated with a magmatic arc as for the Algamarca deposit, the mineralizing fluids are interpreted as acidic and oxidized magmatic fluids, which set high- or intermediate-sulfidation conditions (Hedenquist et al., 2000; Sillitoe and Hedenquist, 2005). The interaction between the oxidized magmatic fluid and the organic matter from the sediments produces fundamental changes in the key parameters of the fluid, i.e., a fluid pH and H_2S concentration increase, and a minor f_{O2} decrease (Vallance et al., 2024). The increase in H_2S and pH both act to enhancing the Au solubility in the form of Au^I hydrosulfide complexes, and is much stronger than the opposite affect produced by f_{O2} decrease, according to the reaction:

$$Au_{(metal)} + ¼ O_2 + 2 H_2S_{(aq)} = Au(HS)_2^- + H^+ + ½ H_2O \qquad (2)$$

Other Au complexes such as those with the radical trisulfur ion, which may be important at higher temperatures and more oxidizing conditions of porphyry deposits ($Au(HS)S_3^-$; Pokrovski et al., 2015), were predicted to be minor in reduced epithermal settings such as that of our study (Vallance et al., 2024). Thus, driven by reaction (2), after the fluid-organic matter interactions, the Au-bearing fluid will continue its ascent to the surface without having lost its gold content. On its route, the fluid can reach structural and/or sedimentary traps, which can promote its accumulation. In these shallower and colder settings, the pyrite can crystallize in optimal conditions to efficiently incorporate both Au and As in its lattice. This is because the near-neutral pH and reduced conditions of the modified fluid favor the incorporation of bound Au and As in pyrite (Pokrovski et al., 2021; Vallance et al., 2024), conditions contrasting to those shown by the original acidic and oxidized magmatic fluids.

The characteristics of mineralizing fluids in sediment-hosted gold deposits of Carlin and orogenic types are similar. They are low salinity fluids, relatively reduced, with a near neutral pH, a ratio $CO_2/CH_4 > 1$ and abundant H_2S (Hofstra and Cline, 2000; Simmons et al., 2020). The fluids, recorded by immiscible-liquid fluid inclusions in the Algamarca veins, have similar characteristics to the fluids found in such sediment-hosted deposits. Indeed, our results show that the interaction of a magmatic fluid with organic matter in a basin can generate fluids like those reported in other sediment-hosted gold deposits.

4.6. Implications for exploration

The Algamarca and Shahuindo epithermal deposits are related to the same magmatic-hydrothermal center (Galdos et al., 2021), and both should be associated with a parental porphyry stock, in a similar way to other examples of porphyry-epithermal systems reported in the MFTB

(e.g., Gustafson et al., 2005; Santos et al., 2023). Our study on the origin of mineralizing fluid and ore mineralogy supports the hypothesis of a hidden porphyry-style mineralization. In the Algamarca veins, uplift and erosion synchronous to the lifespan of the deposit seem to have allowed superposition of a later epithermal stage (stage B) over an earlier porphyry-like stage (stage A). Such telescoping is a common process reported in porphyry systems worldwide (Sillitoe, 2010) and specifically in the MFTB (e. g., Catchpole et al., 2015).

In the Algamarca deposit, the mineralization event defined as stage A is composed mainly of quartz, gold-poor pyrite, and chalcopyrite. This mineral association can correspond to porphyry-type veins. As we determined in stage A, the quartz contains abundant multiphase-solid fluid inclusions. In porphyry deposits, the dense brine liquids remain at depth near the parental porphyry stock (e.g., Lerchbaumer and Audétat, 2012; Rottier et al., 2018). We only recognized stage A in the veins located at the northeast of the Alisos fault, providing an exploration vector toward a porphyry-style mineralization in this direction. In addition, in our study area, the intersection of NW-SE thrust faults or the anticline axis with the younger NE-SW faults that controlled the emplacement of porphyritic stocks has also been evidenced in El Galeno, Michiquillay and Shahuindo deposits within the MFTB (Davies and Williams, 2005; Vallance et al., 2024). Therefore, these intersections may be considered as potential sites for the emplacement of the parental porphyritic stock related to the Algamarca and Shahuindo epithermal mineralizations (Fig. 18).

5. Concluding remarks

We have investigated the Algamarca deposit, which is an epithermal deposit emplaced in a sedimentary basin rich in carbonaceous matter. Mineralogical and geochemical data on ore and gangue minerals were obtained by etching techniques, optical microscopy, scanning electron microscopy, X-ray diffraction, electron microprobe, and LA-ICPMS. Fluid inclusions in quartz were studied by cathodoluminescence, microthermometry, Raman spectroscopy, and LA-ICPMS.

Four stages of mineral precipitation were identified: three hypogene stages, of which the second, labelled as 'the gold stage', contains the major amounts of the metals of interest (Au, Ag, and Cu), while the first and third ('pre- and post-gold stages') events can be considered as non-economic or barren events. The hypogene events were followed by a fourth, supergene event. The main gold stage comprises an invisible-gold sub-stage, which contains mainly quartz and gold-rich arsenian pyrite, and a visible-gold sub-stage containing native gold particles associated with tetrahedrite-tennantite crystals, accompanied by minor chalcopyrite occurrences. Pyrite that occurs in the invisible-gold sub-stage is enriched in both Au and As that were likely incorporated in the pyrite structure via a coupled redox reaction.

Fluid inclusion analyses clearly point to a magmatic origin for the ore-bearing fluid. The fluid is particularly enriched in CO_2, CH_4 and H_2S, providing evidence for strong interactions between the ascending magmatic fluid and carbon-bearing sediments, mainly by reaction of graphite with water to form CO_2 and CH_4.

Interaction between an oxidized magmatic fluid and carbonaceous material from the sediments promotes the transport of gold, following the results of a companion paper (Vallance et al., 2024). Such modified hydrothermal fluids have favorable pH and high H_2S concentrations to efficiently transport dissolved gold as hydrosulfide complexes. Hence, such mineralizing fluids can follow their pathways guided by the thrust-faults system until they reach some structural and/or sedimentary traps in which arsenic-rich pyrite can precipitate due to optimal pH and redox conditions, triggering gold scavenging by the mineral from the fluid.

The differences in ore mineralogy, pyrite composition, and fluid inclusion data between the pre-gold and gold stages are interpreted as a process of telescoping of an epithermal-style overprinting a porphyry-style mineralization, which may be extended to greater depth underneath the sedimentary sequence hosting the epithermal deposit. It

follows that our investigation of the characteristics of the mineralizing fluid and ore minerals can provide a novel targeting tool for exploration of hidden porphyry-style mineralizations.

Declaration of competing interest

Data availability

All data are provided in the manuscript and Supplement Material.

Acknowledgments

Appendix A. Supplementary data

Supplementary data to this article can be found online at https://doi.org/10.1016/j.oregeorev.2023.105857.

References

Aarnes, I., Svensen, H., Connolly, J.A.D., Podlachikov, Y.Y., 2010. How contact metamorphism can trigger climate changes: modelling gas generation around igneous sills in sedimentary basins. Geochim. Cosmochim. Acta 74, 7179–7195.

Agangi, A., Hofmann, A., Wohlgemuth-Ueberwasser, C.C., 2013. Pyrite zoning as a record of mineralization in the Ventersdorp Contact Reef, Witwatersrand Basin, South Africa. Econ. Geol. 108, 1243–1272.

Agangi, A., Hofmann, A., Rollion-Bard, C., Marin-Carbonne, J., Cavalazzi, B., Large, R., Meffre, S., 2015. Gold accumulation in the Archaean Witwatersrand Basin, South Africa—Evidence from concentrically laminated pyrite. Earth Sci. Rev. 140, 27–53.

Akinfiev, N.N., Diamond, L.W., 2003. Thermodynamic description of aqueous nonelectrolytes over a wide range of state parameters. Geochim. Cosmochim. Acta 67, 613–627.

Arehart, G.B., 1996. Characteristics and origin of sediment-hosted disseminated gold deposits: A review. Ore Geol. Rev. 11, 383–403.

Audétat, A., Simon, A.C., 2012. Magmatic controls on porphyry copper genesis. Soc. Econ. Geol. Spec. Publ. 16, 553–572.

Bakker, R.J., 1997. CLATHRATES: computer programs to calculate fluid inclusion V-X properties using clathrate melting temperatures. Comput. Geosci. 23, 1–18.

Bakker, R.J., 2003. Package FLUIDS 1. Computer programs for analysis of fluid inclusion data and for modelling bulk fluid properties. Chem. Geol. 194, 3–23.

Barker, S.L., Hickey, K.A., Cline, J.S., Dipple, G.M., Kilburn, M.R., Vaughan, J.R., Longo, A.A., 2009. Uncloaking invisible gold: Use of nanoSIMS to evaluate gold, trace elements, and sulfur isotopes in pyrite from Carlin-type gold deposits. Econ. Geol. 104, 897–904.

Barré, G., Truche, L., Bazarkina, E.F., Michels, R., Dubessy, J., 2017. First evidence of the trisulfur radical ion S_3^- and other sulfur polymers in natural fluid inclusions. Chem. Geol. 462, 1–14.

Benavides-Cáceres, V., 1956. Cretaceous system in northern Peru. Bull. Am. Mus. Nat. Hist. 108, 352–494.

Benavides-Cáceres, V., 1999. Orogenic evolution of the Peruvian Andes: The Andean cycle. Soc. Econ. Geol. Special Publ. 7, 61–107.

Beyssac, O., Goffé, B., Chopin, C., Rouzaud, J., 2002. Raman spectra of carbonaceous material in metasediments: a new geothermometer. J. Metamorph. Geol. 20, 859–871.

Bissig, T., Tosdal, R.M., 2009. Petrogenetic and metallogenetic relationships in the eastern Cordillera Occidental of central Peru. J. Geol. 117, 499–518.

Bodnar, R.J., 1993. Revised equation and table for determining the freezing point depression of H_2O-NaCl solutions. Geochim. Cosmochim. Acta 57, 683–684.

Bodnar, R.J., Lecumberri-Sanchez, P., Moncada, D., Steele-MacInnis, M., 2014. Fluid inclusions in hydrothermal ore deposits. In: Holland, H.D., Turekian, K.K. (Eds.), Treatise on Geochemistry, , second ed.13. Elsevier, Oxford, pp. 119–142.

Bodnar, R.J., Vityk, M.O., 1994. Interpretation of microthermometric data for H$_2$O-NaCl fluid inclusions. In: De Vivo, B., Frezzotti, M.L. (Eds.), Fluid Inclusions in Minerals, Methods and Applications. Virginia Tech, Blacksburg, Virginia, pp. 117–130.

Burke, E.A.J., 2001. Raman microspectrometry of fluid inclusions. Lithos 55, 139–158.

Campbell, A.R., Robinson-Cook, S., 1987. Infrared fluid inclusion microthermometry on coexisting wolframite and quartz. Econ. Geol. 83, 1640–1645.

Cao, M.J., Qin, K.Z., Li, G.M., Evans, N.J., Jin, L.Y., 2014a. Abiogenic Fischer-Tropsch synthesis of methane at the Baogutu reduced porphyry copper deposit, western Junggar, Nwchina. Geochim. Cosmochim. Acta 141, 179–198.

Cao, M.J., Li, G.M., Qin, K.Z., Jin, L.Y., Evans, N.J., Yang, X.R., 2014b. Baogutu: an example of reduced porphyry Cu deposit in western Junggar. Ore Geol. Rev. 56, 159–180.

Capriolo, M., Marzoli, A., Aradi, L.E., Ackerson, M.R., Bartoli, O., Callegaro, S., Dal Corso, J., Ernesto, M., Gouvêa Vasconcellos, E.M., De Min, A., Newton, R.J., Szabó, C., 2021. Massive methane fluxing from magma-sediment interaction in the end-Triassic central Atlantic magmatic province. Nat. Commun. 12, 5534.

Catchpole, H., Kouzmanov, K., Fontboté, L., Guillong, M., Heinrich, C.A., 2011. Fluid evolution in zoned Cordilleran polymetallic veins—insights from microthermometry and LA-ICPMS of fluid inclusions. Chem. Geol. 281, 293–304.

Catchpole, H., Kouzmanov, K., Putlitz, B., Seo, J.H., Fontboté, L., 2015. Zoned base metal mineralization in a porphyry system: origin and evolution of mineralizing fluids in the Morococha District. Peru. Econ. Geol. 110, 39–71.

Cerpa, L.M., Bissig, T., Kyser, K., McEwan, C., Macassi, A., Rios, H.W., 2013. Lithologic controls on mineralization at the Lagunas Norte high-sulfidation epithermal gold deposit, northern Peru. Miner. Deposita 48, 653–673.

Chew, D., Schaltegger, U., Košler, J., Whitehouse, M.J., Gutjahr, M., Spikings, R.A., Mišković, A., 2007. U-Pb geochronologic evidence for the evolution of the Gondwanan margin of the north central Andes. Geol. Soc. Am. Bull. 119, 697–711.

Cline, J.S., Hofstra, A.H., Muntean, J.L., Tosdal, R.M., Hickey, K.A., 2005. Carlin-type gold deposits in Nevada: critical geologic characteristics and viable models. Econ. Geol. 100, 451–454.

Cooke, D.R., Hollings, P., Walshe, J.L., 2005. Giant porphyry deposits: characteristics, distribution, and tectonic controls. Econ. Geol. 100, 801–818.

Cossio, A., Jaen, H., 1967. Geología de los cuadrángulos de Puémape, Chocope, Otuzo, Trujillo, Salaverry y Santa. Servicio de geología y minería del Perú, Bol. 17. 141 p.

Crede, L.-S., Liu, W., Evans, K.A., Rempel, K.U., Testemale, D., Brugger, J., 2019. Crude oil as ore fluids: An experimental in-situ XAS study of gold partitioning between brine and organic fluid from 25 to 250 °C. Geochim. Cosmochim. Acta 244, 352–365.

Davies, R.C., Williams, P.J., 2005. The El Galeno and Michiquillay porphyry Cu-Au-Mo deposits: Geological descriptions and comparison of Miocene porphyry systems in the Cajamarca district, northern Peru. Miner. Deposita 40, 598–616.

Deditius, A.P., Reich, M., Kesler, S.E., Utsunomiya, S., Chryssoulis, S.L., Walshe, J., Ewing, R.C., 2014. The coupled geochemistry of Au and As in pyrite from hydrothermal ore deposits. Geochim. Cosmochim. Acta 140, 644–670.

Defilippi, C., Muerhoff, C.V., Williams, T., 2016. In: Technical Report on the Shahuindo Mine. NI, Cajabamba, Peru, p. 307.

Ding, Z., Sun, X., Hu, S., Chen, H., Li, D., Fu, Y., Xu, L., Wu, Z., Huang, F., 2023. Role of carbonaceous material in gold precipitation for orogenic gold deposits: A case study of the Bangbu gold deposit in southern Tibet, China. Ore Geol. Rev. 152, 105231.

Dubessy, J., Caumon, M.-C., Rull, F., 2012. Raman spectroscopy applied to earth sciences and cultural heritage. EMU Notes Mineral. 12, 438 p.

Echavarria, L., Nelson, E., Humphrey, J., Chavez, J., Escobedo, L., Iriondo, A., 2006. Geologic evolution of the Caylloma epithermal vein district, southern Peru. Econ. Geol. 101, 843–863.

Emsbo, P., Groves, D.I., Hofstra, A.H., Bierlein, F.P., 2006. The giant Carlin gold province: a protracted interplay of orogenic, basinal, and hydrothermal processes above a lithospheric boundary. Miner. Deposita 41, 517–525.

Eude, A., Roddaz, M., Brichau, S., Brusset, S., Baby, P., Calderon, Y., Soula, J.C., 2015. Timing of exhumation and deformation in the northern Peruvian Eastern Andean Wedge (5–8 S) as inferred from low temperature thermochronology and balanced cross section. Tectonics 34, 715–730.

Fan, H.-R., Xie, Y.-H., Wang, K.-Y., Wilde, S.A., 2004. Methane-rich fluid inclusions in skarn near the giant REE–Nb–Fe deposit at Bayan Obo, northern China. Ore Geol. Rev. 25, 301–309.

Fontboté, L., Kouzmanov, K., Chiaradia, M., Pokrovski, G.S., 2017. Sulfide minerals in hydrothermal deposits. Elements 13, 97–103.

Franchini, M., McFarlane, C., Maydagán, L., Reich, M., Lentz, D.R., Meinert, L., Bouhier, V., 2015. Trace metals in pyrite and marcasite from the Agua Rica porphyry-high sulfidation epithermal deposit, Catamarca, Argentina: textural features and metal zoning at the porphyry to epithermal transition. Ore Geol. Rev. 66, 366–387.

Frezzotti, M.L., Tecce, F., Casagli, A., 2012. Raman spectroscopy for fluid inclusion analysis. J. Geochem. Explor. 112, 1–20.

Frimmel, H.E., Nwaila, G.T., 2020. Geologic evidence of syngenetic gold in the Witwatersrand Goldfields, South Africa. Soc. Econ. Geol. Spec. Publ. 23, 645–668.

Fuchs, S., Schumann, D., Martin, R.F., Couillard, M., 2021. The extensive hydrocarbon-mediated fixation of hydrothermal gold in the Witwatersrand Basin, South Africa. Ore Geol. Rev. 138, 104313.

Gaboury, D., MacKenzie, D., Craw, D., 2021. Fluid volatile composition associated with orogenic gold mineralization, Otago Schist, New Zealand: Implications of H$_2$ and C$_2$H$_6$ for fluid evolution and gold source. Ore Geol. Rev. 133, 104086.

Galdos R., Vallance J., Baby P., Pokrovski G.S., 2021. A common hydrothermal magmatic system generates different styles of gold mineralization at Algamarca and Shahuindo, northern Peru. ProEXPLO 2021, Lima, Peru. Extended Abstracts 100–104.

Gauthier A., Díaz N., Quirita V., 1999. Yacimientos la Arena-Virgen. ProEXPLO 1999, Lima, Perú. Primer volumen de monografías de yacimientos minerales peruanos. Historia, exploración y geología. 73–91.

Ge, X., Shen, C., He, P., Jin, Y., Li, S., Chen, Y., 2022. The roles of hydrocarbons on the mineralization of Carlin-type gold deposits, Nanpanjiang Basin, South China. Ore Geol. Rev. 149, 105107.

Goldstein, R.H., Reynolds, T.J., 1994. Systematics of fluid inclusions in diagenetic minerals. SEPM short course Soc. for Sedimentary Geol. USA, 199 p.

Gregory, D.D., Large, R.R., Halpin, J.A., Lounejeva Baturina, E., Lyons, T.W., Wu, S., Sack, P.J., Chappaz, A., Maslennikov, V.V., Bull, S.W., Danyushevsky, L., 2015. Trace element content of sedimentary pyrite in black shales. Econ. Geol. 110, 1389–1410.

Groves, D.I., Goldfarb, R.J., Robert, F., et al., 2003. Gold deposits in metamorphic belts overview of current understanding, outstanding problems, future research, and exploration significance. Econ. Geol. 98, 1–29.

Guillong, M., Meier, D.L., Allan, M.M., Heinrich, C.A., Yardley, B.W.D., 2008. SILLS: AMATLAB-based program for the reduction of laser ablation ICP-MS data of homogeneous materials and inclusions. Miner. Ass. Can. Short Course Ser. 40, 328–333.

Gustafson, L.B., Vidal, C.E., Pinto, R., Noble, D.C., 2005. Porphyry-epithermal transition, Cajamarca region, northern Peru. Soc. Econ. Geol. Spec. Publ. 11, 279–299.

Harris, A.H., Golding, S.D., White, N.C., 2005. Bajo de la Alumbrera copper–gold deposit: stable isotope evidence for a porphyry-related hydrothermal system dominated by magmatic aqueous fluids. Econ. Geol. 100, 863–886.

Hedenquist, J.W., Arribas, A., Gonzales-Urien, E., 2000. Exploration for epithermal gold deposits. Soc. Econ. Geol. Rev. 13, 245–277.

Heinrich, C.A., Pettke, T., Halter, W.E., Aigner-Torres, M., Audétat, A., Gunther, D., Hattendorf, B., Bleiner, D., Guillong, M., Horn, I., 2003. Quantitative multi-element analysis of minerals, fluid and melt inclusions by LA-ICP-mass spectrometry. Geochim. Cosmochim. Acta 67, 3473–3497.

Hezarkhani, A., Williams-Jones, A.E., Gammons, C.H., 1999. Factors controlling copper solubility and chalcopyrite deposition in the Sungun porphyry copper deposit. Iran. Miner. Deposita 34, 770–783.

Hodder, R.W., Amireault, S., Arsenault, C., Huisa, F., 2010. The Shahuindo epithermal gold occurrence Cajabamba Province, Peru. Petrographic reconnaissance & interpretation of shape and size: Report Prepared for Sulliden Gold Corporation Ltd. 121 p.

Hofstra, A.H., Cline, J.S., 2000. Characteristics and models for Carlin-type gold deposits. Soc. Econ. Geol. Rev. 13, 163–220.

Hu, S., Evans, K., Craw, D., Rempel, K., Bourdet, J., Dick, J., Grice, K., 2015. Raman characterization of carbonaceous material in the Macraes orogenic gold deposit and metasedimentary host rocks, New Zealand. Ore Geol. Rev. 70, 80–95.

Iacono-Marziano, G., Gaillard, F., Scaillet, B., Polozov, A.G., Marecal, V., Pirre, M., Arndt, N., 2012. Extremely reducing conditions reached during basaltic intrusion in organic matter bearing sediments. Earth Planet. Sci. Lett. 357–358, 319–326.

INGEMMET, 2017. Mapa Geológico del Perú, escala 1:100,000. https://geocatmin.ingemmet.gob.pe/geocatmin/.

Ishida, M., Romero, R., Leisen, M., Yasukawa, K., Nakamura, K., Barra, F., Reich, M., Kato, Y., 2021. Auriferous pyrite formed by episodic fluid inputs in the Akeshi and Kasuga high-sulfidation deposits, Southern Kyushu, Japan. Miner. Deposita 57, 129–145.

Jacquemet, N., Guillaume, D., Zwick, A., Pokrovski, G.S., 2014. In situ Raman spectroscopy identification of the S$_3$ ion in S-rich hydrothermal fluids from synthetic fluid inclusions. Amer. Mineral. 99, 1109–1118.

Jaillard, E., Jacay, J., 1989. Les "Couches Chicama" du Nord du Perou: colmatage d'un bassin né d'une collision oblique au tithonique. C.R. Acad. Sci. Paris 308 (II), 1459–1465.

Kendrick, M.A., Burgess, R., Pattrick, R.A.D., Turner, G., 2001. Fluid inclusion noble gas and halogen evidence on the origin of Cu-porphyry mineralizing fluids. Geochim. Cosmochim. Acta 65, 2651–2668.

Kokh, M.A., Lopez, M., Gisquet, P., Lanzanova, A., Candaudap, F., Besson, P., Pokrovski, G.S., 2016. Combined effect of carbon dioxide and sulfur on vapor-liquid partitioning of metals in hydrothermal systems. Geochim. Cosmochim. Acta 187, 311–333.

Kouketsu, Y., Mizukami, T., Mori, H., Endo, S., Aoya, M., Hara, H., Nakamura, D., Wallis, S., 2014. A new approach to develop the Raman carbonaceous material geothermometer for low-grade metamorphism using peak width. Isl. Arc 23, 33–50.

Kouzmanov, K., Pettke, T., Heinrich, C.A., 2010. Direct analysis of ore-precipitating fluids: combined IR microscopy and LA-ICPMS study of fluid inclusions in opaque ore minerals. Econ. Geol. 105, 351–373.

Kouzmanov, K., Pokrovski, G.S., 2012. Hydrothermal controls on metal distribution in porphyry Cu(-Au-Mo) systems. Soc. Econ. Geol. Spec. Publ. 16, 573–618.

Kouzmanov, K., Bailly, L., Ramboz, C., Rouer, O., Beny, J.M., 2002. Morphology, origin and infrared microthermometry of fluid inclusions in pyrite from the Radka epithermal copper deposit, Srednogorie zone, Bulgaria. Miner. Deposita 37, 599–613.

Kretschmar, U., Scott, S.D., 1976. Phase relations involving arsenopyrite in the system Fe-As-S and their application. Can. Miner. 14, 364–386.

Kusebauch, C., Oelze, M., Gleeson, S.A., 2018. Partitioning of arsenic between hydrothermal fluid and pyrite during experimental siderite replacement. Chem. Geol. 500, 136–147.

Kusebauch, C., Gleeson, S.A., Oelze, M., 2019. Coupled partitioning of Au and As into pyrite controls formation of giant Au deposits. Sci. Adv. 5, eaav5891.

Lahfid, A., Beyssac, O., Deville, E., Negro, F., Chopin, C., Goffé, B., 2010. Evolution of the Raman spectrum of carbonaceous material in low grade metasediments of the Glarus Alps (Switzerland). Terra Nova 22, 354–360.

Lang, X., Deng, Y., Wang, X., Tang, J., Xie, F., Yang, Z., Jiang, K., 2020. Reduced fluids in porphyry copper-gold systems reflect the occurrence of the wall-rock thermogenic process: An example from the No. 1 deposit in the Xiongcun district, Tibet, China. Ore Geol. Rev. 118, 103212.

Large, R.R., Bull, S.W., Maslennikov, V.V., 2011. A carbonaceous sedimentary source-rock model for carlin-type and orogenic gold deposits. Econ. Geol. 106, 331–358.

Large, R.R., Meffre, S., Burnett, R., Guy, B., Bull, S., Gilbert, S., Goemann, K., Danyushevsky, L., 2013. Evidence for an intra basinal source and multiple concentration processes in the formation of the carbon leader reef, Witwatersrand Supergroup, South Africa. Econ. Geol. 108, 1215–1241.

Large, S.J.E., Bakker, E.Y.N., Weis, P., Wälle, M., Ressel, M., Heinrich, C.A., 2016. Trace elements in fluid inclusions of sediment-hosted gold deposits indicate a magmatic-hydrothermal origin of the Carlin ore trend. Geology 44, 1015–1018.

Lerchbaumer, L., Audétat, A., 2012. High Cu concentrations in vapor-type fluid inclusions: An artifact? Geochim. Cosmochim. Acta 88, 255–274.

Lowenstern, J.B., 2001. Carbon dioxide in magmas and implications for hydrothermal systems. Miner. Deposita 36, 490–502.

Magoon, L.B., Dow, W.G., 1994. The petroleum system. AAPG Mem. 60, 3–24.

Mégard, F., 1984. The Andean orogenic period and its major structures in central and northern Perú. J. Geol. Soc. Lond. 141, 893–900.

Migdisov, A.A., Guo, X., Williams-Jones, A.E., Sun, C.J., Vasyukova, O., Sugiyama, I., Fuchs, S., Pearce, K., Roback, R., 2017. Hydrocarbons as ore fluids: Geochem. Persp. Let. 5, 47–52.

Minissale, A., Kerrick, D.M., Magro, G., Murrell, M.T., Paladini, M., Rihs, S., Sturchio, N. C., Tassi, F., Vaselli, O., 2002. Geochemistry of Quaternary travertines in the region north of Rome (Italy): structural, hydrologic and paleoclimatic implications. Earth Planet. Sci. Lett. 203, 709–728.

Montgomery, A.T., 2012. Metallogenetic controls on Miocene high-sulphidation epithermal gold mineralization, Alto Chicama district, La Libertad, northern Perú. Queen's University, Kingston, Ontario, Canada, p. 381. Unpublished PhD thesis.

Moritz, R., 2006. Fluid salinities obtained by infrared microthermometry of opaque minerals: implications for ore deposit modeling—a note of caution. J. Geochem. Explor. 89, 284–287.

Muntean, J.L., Cline, J.S., Simon, A.C., Longo, A.A., 2011. Magmatic-hydrothermal origin of Nevada's Carlin-type gold deposits. Nature 4, 122–127.

Nahnybida, T., Gleeson, S.A., Rusk, B.G., Wassenaar, L.I., 2009. Cl/Br ratios and stable chlorine isotope analysis of magmatic–hydrothermal fluid inclusions from Butte, Montana and Bingham Canyon. Utah. Miner. Deposita 44, 837–848.

Naumov, G.B., Ryzhenko, B.N., Khodakovsky, I.L., 1971. Handbook of thermodynamic data. Atomizdat, Moscow (in Russian). English translation is available from U.S. Department of Commerce, Washington D.C., PB-226.

Navarro C.P., Rivera P.M., Monge M. R., 2010. Geología y metalogenia del Grupo Calipuy (Volcanismo Cenozoico) Segmento Santiago de Chuco, norte del Perú: Ministerio de Energía y Minas INGEMMET, Boletín N ° 28 Serie D, Estudios Regionales, 201 p.

Noble, D.C., McKee, E.H., 1999. The Miocene metallogenic belt of central and northern Peru. in: Skinner, B.J. (Ed.), Geology and Ore Deposits of the central Andes. Soc. Econ. Geol. Spec. Publ. 7, 155–193.

Noble, D.C., McKee, E.H., Mégard, F., 1979. Early Tertiary "Incaic" tectonism, uplift, and volcanic activity, Andes of central Peru. Geol. Soc. Am. Bull. 90, 903–907.

Noble, D.C., McKee, E.H., Mourier, T., Mégard, F., 1990. Cenozoic stratigraphy, magmatic activity, compressive deformation and uplift in northern Peru. Geol. Soc. Am. Bull. 102, 1105–1113.

Norman, M.D., Pearson, N.J., Sharma, A., Griffin, W.L., 1996. Quantitative analysis of trace elements in geological materials by laser ablation ICP-MS: Instrumental operating conditions and calibration values of NIST glasses. Geostand. Newslett. 20, 247–261.

Ortelli, M., Kouzmanov, K., Wälle, M., Ubrig, N., Casanova, V., 2018. Fluid inclusion studies in opaque ore minerals: I. Trace element content and physical properties of ore minerals controlling textural features in transmitted near-infrared light microscopy. Econ. Geol. 113, 1845–1860.

Pinet, N., Haeri-Ardakani, O., Jautzy, J., Savard, M.M., Sack, P., Mercier-Langevin, P., 2023. Thermal history of Carlin-type gold deposits in Yukon (Canada) as revealed by organic matter geothermometry, clumped isotope data, fluid inclusion microthermometry, and apatite fission-track analyses. Miner. Deposita 58, 903–923.

Pokrovski, G.S., Gout, R., Schott, J., Zotov, A., Harrichoury, J.C., 1996. Thermodynamic properties and stoichiometry of As(III) hydroxide complexes at hydrothermal solutions. Geochim. Cosmochim. Acta 60, 737–749.

Pokrovski, G.S., Kara, S., Roux, J., 2002. Stability and solubility of arsenopyrite, FeAsS, in crustal fluids. Geochim. Cosmochim. Acta 66, 2361–2378.

Pokrovski, G.S., Borisova, A.Y., Bychkov, A.Y., 2013. Speciation and transport of metals and metalloids in geological vapors. Rev. Miner. Geochem. 76, 165–218.

Pokrovski, G.S., Akinfiev, N.N., Borisova, A.Y., Zotov, A.V., Kouzmanov, K., 2014. Gold speciation and transport in geological fluids: insights from experiments and physical-chemical modeling. In: Garofalo, P., Ripley, E. (Eds.), Gold-Transporting Fluids in the Earth's Crust, Geol. Soc. London Spec. Publ., 402, pp. 9–70.

Pokrovski, G.S., Dubessy, J., 2015. Stability and abundance of the trisulfur radical ion S_3^- in hydrothermal fluids. Earth Planet. Sci. Lett. 411, 298–309.

Pokrovski, G.S., Kokh, M.A., Guillaume, D., Borisova, A.Y., Gisquet, P., Hazemann, J.-L., Lahera, E., Del Net, W., Proux, O., Testemale, D., Haigis, V., Jonchière, R., Seitsonen, A.P., Ferlat, G., Vuilleumier, R., Saitta, A.M., Boiron, M.-C., Dubessy, J., 2015. Sulfur radical species form gold deposits on Earth. Proc. Nat. Acad. Sci. USA (PNAS) 112 (44), 13484–13489.

Pokrovski, G.S., Escoda, C., Blanchard, M., Testemale, D., Hazemann, J.L., Gouy, S., Kokh, M.A., Boiron, M.-C., Parseval, F., Aigouy, T., Menjot, L., de Parseval, P., Proux, O., Rovezzi, M., Béziat, D., Salvi, S., Kouzmanov, K., Bartsch, T., Pöttgen, R.,

Doert, T., 2021. An arsenic-driven pump for invisible gold in hydrothermal systems. Geochem. Persp. Let. 17, 39–44.

Potter II, W.R., Brown, D.L., 1977. The volumetric properties of aqueous sodium chloride solutions from 0° to 500 °C at pressures up to 2000 bars based on a regression of available data in the literature. U.S. Geol. Survey Bull. 1421-c, 36 p.

Prudhomme, A., Baby, P., Robert, A., Brichau, S., Cuipa, E., Eude, A., Calderon, Y., O'Sullivan, P., 2019. Western thrusting and uplift in northern central Andes (western Peruvian margin). In: Horton, B.K., Folguera, A. (Eds.), Andean Tectonics. Elsevier, Amsterdam, pp. 299–331.

Radtke, A.S., Scheiner, B.J., 1970. Studies of hydrothermal gold deposition (I). Carlin gold deposit, Nevada: The role of carbonaceous materials in gold deposition. Econ. Geol. 65, 87–102.

Rahl, J.M., Anderson, K.M., Brandon, M.T., Fassoulas, C., 2005. Raman spectroscopic carbonaceous material thermometry of low-grade metamorphic rocks: calibration and application to tectonic exhumation in Crete, Greece. Earth Planet. Sci. Lett. 240, 339–354.

Rainbow, A., Clark, A.H., Kyser, T.K., Gaboury, F., Hodgson, C.J., 2005. The Pierina epithermal Au–Ag deposit, Ancash, Peru: paragenetic relationships, alunite textures, and stable isotope geochemistry. Chem. Geol. 215, 235–252.

Rauchenstein-Martinek, K., Wagner, T., Wälle, M., Heinrich, C.A., Arlt, T., 2016. Chemical evolution of metamorphic fluids in the Central Alps, Switzerland: insight from LA-ICPMS analysis of fluid inclusions. Geofluids 16, 877–908.

Reich, M., Kesler, S.E., Utsunomiya, S., Palenik, C.S., Chryssoulis, S.L., Ewing, R., 2005. Solubility of gold in arsenian pyrite. Geochim. Cosmochim. Acta 69, 2781–2796.

Richards, J.P., Kerrich, R., 1993. Observations of zoning and fluid inclusions in pyrite using a transmitted infrared light microscope (Lambda< or= 1.9 mu m). Econ. Geol. 88, 716–723.

Rosenbaum, G., Giles, D., Saxon, M., Betts, P.G., Weinberg, R.F., Duboz, C., 2005. Subduction of the Nazca Ridge and the Inca Plateau: insights into the formation of ore deposits in Peru. Earth Planet. Sci. Lett. 239, 18–32.

Rottier, B., Kouzmanov, K., Walle, M., Bendezú, R., Fontbote, L., 2016a. Sulfide replacement processes revealed by textural and LA-ICPMS trace element analyses: Example from the early mineralization stages at Cerro de Pasco, Peru. Econ. Geol. 111, 1347–1367.

Rottier, B., Kouzmanov, K., Bouvier, A.S., Baumgartner, L.P., Wälle, M., Rezeau, H., Bendezú, R., Fontboté, L., 2016b. Heterogeneous melt and hypersaline liquid inclusions in shallow porphyry type mineralization as markers of the magmatic-hydrothermal transition (Cerro de Pasco district, Peru). Chem. Geol. 447, 93–116.

Rottier, B., Kouzmanov, K., Casanova, V., Wälle, M., Fontboté, L., 2018. Cyclic dilution of magmatic metal-rich hypersaline fluids by magmatic low-salinity fluid: A major process generating the giant epithermal polymetallic deposit of Cerro de Pasco, Peru. Econ. Geol. 113, 825–856.

Rusk, B.G., Reed, M.H., Dilles, J.H., 2008. Fluid inclusion evidence formagmatic–hydrothermal fluid evolution in the porphyry copper–molybdenum deposit at Butte, Montana. Econ. Geol. 103, 307–334.

Samson, I.M., Williams-Jones, A.E., Ault, K.M., Gagnon, J.E., Fryer, B.J., 2008. Source of fluids forming distal Zn–Pb–Ag skarns: evidence from laser ablation-inductively coupled plasma-mass spectrometry analysis of fluid inclusions from El Mochito, Honduras. Geology 36, 947–950.

Santos, A., Guo, W., Chen, N., Cerpa, L., Kojima, S., 2023. Geochronologically constrained life cycles of telescoped porphyry-epithermal systems at the La Arena district, northern Peru. Ore Geol. Rev. 155, 105375.

Scherrenberg, A.F., Kohn, B.P., Holcombe, R.J., Rosenbaum, G., 2016. Thermotectonic history of the Marañón Fold-Thrust Belt, Peru: Insights into mineralisation in an evolving orogen. Tectonophysics 667, 16–36.

Schirra, M., Laurent, O., Zwyer, T., Driesner, T., Heinrich, C.A., 2022. Fluid evolution at the Batu Hijau porphyry Cu-Au deposit, Indonesia: hypogene sulfide precipitation from a single-phase aqueous magmatic fluid during chlorite–white-mica alteration. Econ. Geol. 117, 979–1012.

Seltmann, R., Goldfarb, R.J., Zu, B., Creaser, R.A., Dolgopolova, A., Shatov, V.V., 2020. Muruntau, Uzbekistan: the world's largest epigenetic gold deposit. Soc. Econ. Geol. Spe. Publ. 23, 497–521.

Shen, P., Shen, Y.C., Wang, J.B., Zhu, H.P., Wang, L.J., Meng, L., 2010. Methane-rich fluid evolution of the Baogutu porphyry Cu–Mo–Au deposit, Xinjiang, NW China. Chem. Geol. 275, 78–98.

Shepherd, T.J., Rankin, A.H., Alderton, D.H.M., 1985. A Practical Guide to Fluid Inclusion Studies. Blackie, Glasgow, p. 239.

Sillitoe, R.H., 2010. Porphyry copper systems. Econ. Geol. 105, 3–41.

Sillitoe, R.H., Bonham, H.F., 1990. Sediment-hosted gold deposits: distal products of magmatic-hydrothermal systems. Geology 18, 157–161.

Sillitoe, R.H., Hedenquist, J.W., 2005. Linkages between volcanic tectonic settings, ore fluid compositions, and epithermal precious metals deposits. Soc. Econ. Geol. Spec. Publ. 10, 315–343.

Simmons, S.F., Tutolo, B.T., Barker, S.L.L., Goldfarb, R.J., Robert, F., 2020. Hydrothermal gold deposition in epithermal, Carlin, and orogenic deposits. Soc. Econ. Geol. Spec. Publ. 23, 823–845.

Simmons, S., White, N., John, D., 2005. Geological characteristics of epithermal precious and base metal deposits. Econ. Geol. 100th anniversary, 485–522.

Sośnicka, M., Lüders, V., Duschl, F., Kraemer, D., Laurent, O., Niedermann, S., Banks, D. A., Wilke, F., Wohlgemuth-Ueberwasser, C., Wiedenbeck, M., 2023. Metal budget and origin of aqueous brines depositing deep-seated Zn-Pb mineralization linked to hydrocarbon reservoirs, north German Basin. Miner. Deposita 58, 1143–1170.

Sykora, S., Cooke, D., Meffre, S., Stephanov, A., Gardner, K., Scott, R., Selley, D., Harris, A., 2018. Evolution of pyrite trace element compositions from porphyry-style and epithermal conditions at the Lihir gold deposit: Implications for ore genesis and mineral processing. Econ. Geol. 113, 193–208.

Sylvester, P., Cabri, L.J., Tubrett, M., McMahon, G., Laflamme, J., Peregoedova, A., 2005. Synthesis and evaluation of a fused pyrrhotite standard reference material for platinum group elements and gold analysis by laser ablation-ICP-MS: 10th International Platinum Symposium: Oulu. Geologocal Survey of Finland, Extended Abstracts, pp. 16–20.

Tanner, D., Henley, R.W., Mavrogenes, J.A., Holden, P., 2016. Sulfur isotope and trace element systematics of zoned pyrite crystals from the El Indio Au–Cu–Ag deposit, Chile. Contrib. Mineral Petrol. 171, 1–17.

Tietz, P., Defilippi, C., 2012. Technical Report on the Shahuindo Project, Cajabamba, Peru: NI 43–101. Technical Report Sulliden Gold Corporation LTD, p. 149.

Touray, J.-C., Guilhaumou, N., 1984. Characterization of H_2S-bearing fluid inclusions. Bull. Minéral. 107, 181–188.

Ueno, Y., Yamada, K., Yoshida, N., Maruyama, S., Isozaki, Y., 2006. Evidence from fluid inclusions for microbial methanogenesis in the early Archaean era. Nat. Lett. 440, 516–519.

Vallance, J., Cathelineau, M., Boiron, M., Fourcade, S., Shepherd, T., Naden, J., 2003. Fluid-rock interactions and the role of late Hercynian aplite intrusion in the genesis of the Castromil gold deposit, northern Portugal. Chem. Geol. 194, 201–224.

Vallance, J., Galdos, R., Balboa, M., Berna, B., Cabrera, O., Huisa, F., Baya, C., Van De Vyver, C., Viveen, W., Béziat, D., Salvi, S., Brusset, S., Baby, P., Pokrovski, G.S., 2024. Combined effect of organic carbon and arsenic on the formation of sediment-hosted gold deposits: a case study of the Shahuindo epithermal deposit, Peru. Econ. Geol. (in press).

Van Daele, J., Hulsbosch, N., Dewaele, S., Boiron, M.C., Piessens, K., Boyce, A., Muchez, P., 2018. Mixing of magmatic-hydrothermal and metamorphic fluids and the origin of peribatholitic Sn vein-type deposits in Rwanda. Ore Geol. Rev. 101, 481–501.

Vaughan, J., Nelson, C.E., Polanco, J., Garcia, V., Macassi, A., Garrido, G., 2020. The Pueblo Viejo Au-Ag-Cu-(Zn) deposit, Dominican Republic. Soc. Econ. Geol. Special Publ. 23, 415–430.

Velásquez, G., Béziat, D., Salvi, S., Siebenaller, L., Borisova, A.Y., Pokrovski, G.S., de Parseval, P., 2014. Formation and deformation of pyrite and implications for gold mineralization at the El Callao mining district, Venezuela. Econ. Geol. 109, 457–486.

Vikentyev, I.V., Tyukova, E.E., Vikent'Eva, O.V., Chugaev, A.V., Dubinina, E.O., Prokofiev, V.Y., Murzin, V.V., 2019. Vorontsovka Carlin-style gold deposit in the North Urals: Mineralogy, fluid inclusion and isotope data for genetic model. Chem. Geol. 508, 144–166.

Vursiy, G.L., Zibrov, I.A., Lobov, S.G., Yakubchuk, A.S., 2020. The Sukhoi Log gold deposit, Russia. Soc. Econ. Geol. Spec. Publ. 23, 523–543.

Warr, L.N., 2021. IMA–CNMNC approved mineral symbols. Mineral. Mag. 85, 291–320.

White, N.C., Hedenquist, J.W., 1995. Epithermal gold deposits: styles, characteristics and exploration. Soc. Econ. Geol. Newsletter. 23, 1–13.

Williams-Jones, A.E., Samson, I.M., Ault, K.M., Gagnon, J.E., Fryer, B.J., 2010. The genesis of distal zinc skarns: evidence from the Mochito deposit. Honduras. Econ. Geol. 105, 1411–1440.

Wilson, S.A., Ridley, W.I., Koenig, A.E., 2002. Development of sulfide calibration standards for the laser ablation inductively-coupled plasma mass spectrometry technique. J. Anal. at. Spectrom. 17, 406–409.

Wojdyr, M., 2010. Fityk: a general-purpose peak fitting program. J. Appl. Cryst. 43, 1126–1128.

Wright, P., Melnyk, P., Gomerly, L., Lupo, J., 2009. Shahuindo Gold projet Cajabamba Province, Peru, NI 43–101. Technical report on preliminary assessment prepared for Sulliden Gold Corporation Ltd, p. 196.

Wu, Y.F., Li, J.W., Evans, K., Koenig, A.E., Li, Z.K., O'Brien, H., Lahaye, Y., Rempel, K., Hu, S.Y., Zhang, Z.P., Yu, J.P., 2018. Ore-forming processes of the Daqiao epizonal orogenic gold deposit, West Qinling orogen, China: constraints from textures, trace elements, and sulfur isotopes of pyrite and marcasite, and Raman spectroscopy of carbonaceous material. Econ. Geol. 113, 1093–1132.

Wu, Y.F., Evans, K., Li, J.W., Fougerouse, D., Large, R., Guagliardo, P., 2019. Metal remobilization and ore-fluid perturbation during episodic replacement of auriferous pyrite from an epizonal orogenic gold deposit. Geochim. Cosmochim. Acta 245, 98–117.

Wu, Y.F., Evans, K., Fisher, L.A., Zhou, M.F., Hu, S.Y., Fougerouse, D., Large, R., Li, J.W., 2020. Distribution of trace elements between carbonaceous matter and sulfides in a sediment-hosted orogenic gold system. Geochim. Cosmochim Acta 276, 345–362.

Zajacz, Z., Candela, P.A., Piccoli, P.M., 2017. The partitioning of Cu, Au and Mo between liquid and vapor at magmatic temperatures and its implications for the genesis of magmatic-hydrothermal ore deposits. Geochim. Cosmochim. Acta 207, 81–101.

Zhang, D.H., Audétat, A., 2023. A plea for more skepticism toward fluid inclusions: Part I. Post-entrapment changes in fluid density and fluid salinity are very common. Econ. Geol. 118, 15–41.

Zhang, Y.G., Frantz, J.D., 1987. Determination of homogenization temperatures and densities of supercritical fluids in the system $NaCl–KCl–CaCl_2–H_2O$ using synthetic fluid inclusions. Chem. Geol. 64, 335–350.

Zhang, W., Williams-Jones, A.E., Leng, C.-B., Zhang, X.-C., Chen, W.T., Su, C.-J., Qin, W.-C., Yan, J.-H., 2019. The origin of CH_4-rich fluids in reduced porphyry–skarn Cu–Mo–Au systems. Ore Geol. Rev. 114, 103135.

Zhao, Z.-H., Ni, P., Sheng, Z.-L., Dai, B.-Z., Wang, G.-G., Ding, J.-Y., Wang, B.-H., Zhang, H.-D., Pan, J.-Y., Li, S.-N., 2020. Thermal regime reconstruction and fluid inclusion LA–ICP–MS analysis on intermediate-sulfidation epithermal Pb–Zn veins: Implications for porphyry Cu deposits exploration in the Xianhualing District, Anhui, China. Ore Geol. Rev. 124, 103658.

Zhu, M.T., Wu, G., Xie, H.J., Liu, J., Mi, M., 2012. Geochronology and fluid inclusion studies of the Lailisigaoer and Lamasu porphyry–skarn Cu–Mo deposits in northwestern Tianshan, China. J. Asian Earth Sci. 49, 116–130.

Zotov, A.V., Shikina, N.D., Akinfiev, N.N., 2003. Thermodynamic properties of the Sb(III) hydroxide complex $Sb(OH)_{3(aq)}$ at hydrothermal conditions. Geochim. Cosmochim. Acta 67, 1821–1836.

Zou, H., Li, M., Bagas, L., Li, Y., Fang, Y., Cao, H.W., Jiang, X.W., Chen, H.F., 2020. Fluid composition and evolution of the Langxi Ba-F deposit, Yangtze Block, China: New Insight from LA-ICPMS study of individual fluid inclusion. Ore Geol. Rev. 125, 103702.